

pubs.acs.org/JACS

³¹P Nuclear Magnetic Resonance Spectroscopy as a Probe of Thorium—Phosphorus Bond Covalency: Correlating Phosphorus Chemical Shift to Metal—Phosphorus Bond Order

Jingzhen Du, Joseph Hurd, John A. Seed, Gábor Balázs, Manfred Scheer, Ralph W. Adams,* Daniel Lee,* and Stephen T. Liddle*



Cite This: J. Am. Chem. Soc. 2023, 145, 21766-21784



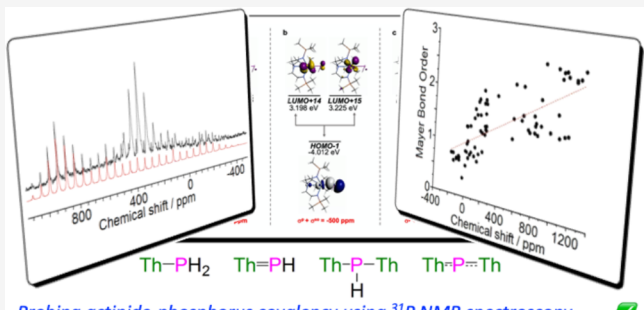
ACCESS I

III Metrics & More

Article Recommendations

Supporting Information

ABSTRACT: We report the use of solution and solid-state ³¹P Nuclear Magnetic Resonance (NMR) spectroscopy combined with Density Functional Theory calculations to benchmark the covalency of actinide-phosphorus bonds, thus introducing 31P NMR spectroscopy to the investigation of molecular f-element chemical bond covalency. The ³¹P NMR data for $[Th(PH_2)-(Tren^{TIPS})]$ (1, $Tren^{TIPS} = \{N(CH_2CH_2NSiPr_3^i)_3\}^{3-})$, $[Th(PH)-(Tren^{TIPS})][Na(12C4)_2]$ (2, 12C4 = 12-crown-4 ether), $[\{Thres_{TIPS}, Tree_{TIPS}, Tree_{TIPS},$ $(\text{Tren}^{\text{TIPS}})$ ₂ $(\mu$ -PH)] (3), and $[\{\text{Th}(\text{Tren}^{\text{TIPS}})\}_2(\mu$ -P)][Na- $(12\text{C4})_2$] (4) demonstrate a chemical shift anisotropy (CSA) ordering of $(\mu - P)^{3-} > (=PH)^{2-} > (\mu - PH)^{2-} > (-PH_2)^{1-}$ and for 4 the largest CSA for any bridging phosphido unit. The B3LYP functional with 50% Hartree-Fock mixing produced spin-orbit



Probing actinide-phosphorus covalency using ³¹P NMR spectroscopy. Correlating ³¹P isotropic chemical shift to metal-phosphorus bond order.

 $\delta_{
m iso}$ values that closely match the experimental data, providing experimentally benchmarked quantification of the nature and extent of covalency in the Th-P linkages in 1-4 via Natural Bond Orbital and Natural Localized Molecular Orbital analyses. Shielding analysis revealed that the 31 P δ_{iso} values are essentially only due to the nature of the Th-P bonds in 1-4, with largely invariant diamagnetic but variable paramagnetic and spin-orbit shieldings that reflect the Th-P bond multiplicities and s-orbital mediated transmission of spin-orbit effects from Th to P. This study has permitted correlation of Th-P δ_{iso} values to Mayer bond orders, revealing qualitative correlations generally, but which should be examined with respect to specific ancillary ligand families rather than generally to be quantitative, reflecting that 31 P δ_{iso} values are a very sensitive reporter due to phosphorus being a soft donor that responds to the rest of the ligand field much more than stronger, harder donors like nitrogen.

INTRODUCTION

A longstanding central challenge in actinide (An) chemistry, and indeed across the periodic table, is reliably determining the extent and nature of covalency in An-ligand bonds. 1-3 This has prompted extensive studies of An-ligand multiple bonds since, apart from realizing novel new structural linkages to compare with long-standing transition metal analogues, arguably An-ligand multiple bonds inherently exhibit the maximum potential for covalency that is amenable to practical study. 4-9 However, while the fundamentals of Pauling's model of chemical bonding are straightforward to grasp, 10 the fine detail is difficult to probe experimentally. Nevertheless, in recent years with ever improving experimental, analytical, and computational methods becoming available, significant advances have been made experimentally probing An-covalency, when underpinned by quantum chemical calculations, 11 including X-ray absorption spectroscopy, 12-20 pulsed electron paramagnetic resonance spectroscopy, ²¹ and nuclear magnetic resonance (NMR) spectroscopy. ^{22,23}

Where the use of NMR spectroscopy to probe An-ligand covalency is concerned, solution and solid-state (SS) studies include ${}^{1}H$, 24,25 ${}^{13}C$, ${}^{25-34}$ ${}^{15}N$, ${}^{35-37}$ ${}^{17}O$, ${}^{38-41}$ ${}^{19}F$, ${}^{42-45}$ ${}^{29}Si$, 46 $^{35/37}$ Cl, 47 77 Se, 48 and 125 Te 48 nuclei, which when taken together has revealed an intimate relationship between chemical shift (δ) properties and the nature of the An-ligand bond. This in turn can afford in-depth information about shielding (σ) tensors and hence the ability to experimentally benchmark and probe An-ligand bonding and thus covalency in great detail. However, one nucleus conspicuous by its absence to date in molecular f-element NMR covalency studies is ³¹P, which is surprising given that ^{31}P is a 100% abundant I = 1/2 nucleus

Received: March 16, 2023 Published: September 28, 2023





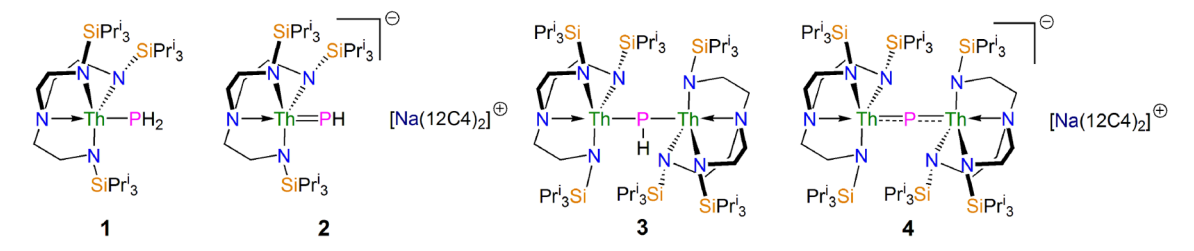


Figure 1. Complexes 1-4.

Table 1. Experimental and Computed NMR Properties for 1-4 and 1'-4'a

Property	1	2	3	4	1'	2′	3′	4′
$\delta_{ m iso(sol)}^{b}$	-144.1^{d}	198.8	145.7	553.5	_	_	_	_
$\delta_{\mathrm{iso(ss)}}^{c}$	-138.9^{d}	211.8	151.8	554.8	_	_	_	_
$\delta_{ m iso(calc)}$	-146.8	216.6	147.8	519.2	-149.9	209.0	167.5	551.1
$\delta_{11(\mathrm{ss})}^{e}$	-83.7	539.9	441.3	1047.2	_	_	_	_
$\delta_{22(\mathrm{ss})}^{e}$	-102.3	368.6	290.8	972.0	_	_	_	_
$\delta_{33(\mathrm{ss})}{}^{e}$	-233.1	-274.6	-279.1	-357.2	_	_	_	_
$\Omega_{(ss)}^{e}$	149.4	813.6	720.5	1404.4	_	_	_	_
$\kappa_{(ss)}^{e}$	0.75	0.58	0.58	0.89	_	_	_	_
$\delta_{11 ext{(calc)}}$	-92.9	523.2	584.6	996.4	-90.6	511.8	589.4	1033.6
$\delta_{22 ext{(calc)}}$	-142.5	404.4	130.7	959.3	-148.5	399.3	160.4	1011.3
$\delta_{33 ext{(calc)}}$	-205.1	-277.7	-271.9	-398.1	-210.5	-284.1	-247.3	-391.8
$\Omega_{ m (calc)}$	112.2	800.9	856.5	1394.5	119.9	795.9	836.7	1425.4
$\kappa_{(\mathrm{calc})}$	0.11	0.70	0.06	0.95	0.04	0.72	0.03	0.97
$\sigma_{ m iso(calc)}$	491.3	127.9	196.7	-174.7	494.4	135.5	177.0	-206.6
$\sigma^{ m d}_{ m (calc)}$	963.2	968.7	968.5	973.9	963.4	969.2	969.5	974.9
$\sigma^{ m p}_{ m (calc)}$	-452.0	-823.7	-663.7	-993.9	-454.3	-817.9	-670.0	-1008.9
$\sigma^{ m so}{}_{ m (calc)}$	-20.0	-17.1	-108	-154.1	-14.7	-15.8	-122.5	-172.5

 a Calculations at the B3LYP-HF50 TZ2P all-electron ZORA spin—orbit (SOR) level in a benzene solvent continuum and corrected for a $\sigma_{\rm iso(calc)}$ of 584.5 ppm for PH₃ noting experimental δ_{iso} values of -266.1 and -240 ppm in the gas-phase and solution (C_6D_6); all δ and σ values are in ppm. Fin C₆D₆. SS-MAS conditions. Average of two molecules. Derived from simulation of the respective experimental SS-MAS ³¹P NMR spectrum.

and hence an extremely attractive and prevalent nucleus for NMR studies generally. However, the notable absence of ³¹P NMR covalency studies in the molecular An domain to date could be that in Hard-Soft Acid-Base (HSAB) theory Ans and P are hard and soft nuclei, respectively, and thus poorly matched, a situation exacerbated when considering that metal-ligand multiple bond systems usually by definition require metal centers in mid- to high-oxidation states (typically +4 to +6) which increases their hardness. It is also the case that many An complexes are paramagnetic, so the range of diamagnetic An-P derivatives is relatively limited, and although Th(IV) is diamagnetic, its bonding is usually more ionic than that of, for example, U, and hence synthesizing and isolating stable Th-ligand multiple bond linkages is often more challenging for the larger Th compared to U on HSAB and steric reasons. Furthermore, to realistically use ³¹P NMR spectroscopy for covalency studies a family of related molecules with varied An-P bond types is required to rigorously construct the necessary framework approach where a single molecular example would not suffice, and there are relatively few complexes with direct An-P bonds that can be described as meeting that criterion. 49-71 It is also the case that An-P bonds are generally prone to decomposition in the presence of air or moisture, making studies more experimentally challenging to undertake. Lastly, another challenge of incorporating ³¹P NMR as a tool for studying An-covalency is that the ³¹P nucleus is exceedingly sensitive to its environment (bond lengths, hybridization, molecular

dynamics, formal molecule charge, phase, solvent), which can render rigorous and systematic understanding challenging to acquire, 72 again highlighting the need for structurally related An-P molecules from which to validate the use of ³¹P NMR spectroscopy in probing covalency.

Germane to the aforementioned arguments, we previously reported a family of triamidoamine-Th complexes with a range of Th-P linkages.^{52a} Specifically, we reported the phosphanide $[Th(PH_2)(Tren^{TIPS})]$ (1, $Tren^{TIPS} = \{N-1\}$ (CH₂CH₂NSiPrⁱ₃)₃}³⁻), the phosphinidene [Th(PH)- $(Tren^{TIPS})][Na(12C4)_2]$ (2, 12C4 = 12-crown-4 ether), the phosphinidiide [{Th(Tren^{TIPS})}₂(μ -PH)] (3), and the bridging phosphido $[{Th(Tren^{TIPS})}_2(\mu-P)][Na(12C4)_2]$ (4), Figure 1. Given our prior work probing the covalency of a terminal uranium(VI)-nitride linkage,³⁷ and introducing ²⁹Si NMR spectroscopy to probing the covalency of lanthanide and s-block silanides, 46 we identified that 1-4 would be an ideal family of molecules with which to probe and benchmark the covalency of the Th-P linkages using ³¹P NMR spectroscopy.

Here, we introduce ³¹P NMR spectroscopy to investigate molecular f-element covalency by the study of the Th-P linkages of 1-4 using solution and SS-Magic Angle Spinning (SS-MAS) NMR techniques. Through this combined approach, underpinned by quantum chemical techniques, we have been able to relate the isotropic chemical shift (δ_{iso}) to its constituent individual components and then relate it to the shielding tensors and hence the Th-P covalency. A combined Molecular Orbital (MO), Natural Bond Orbital (NBO), and

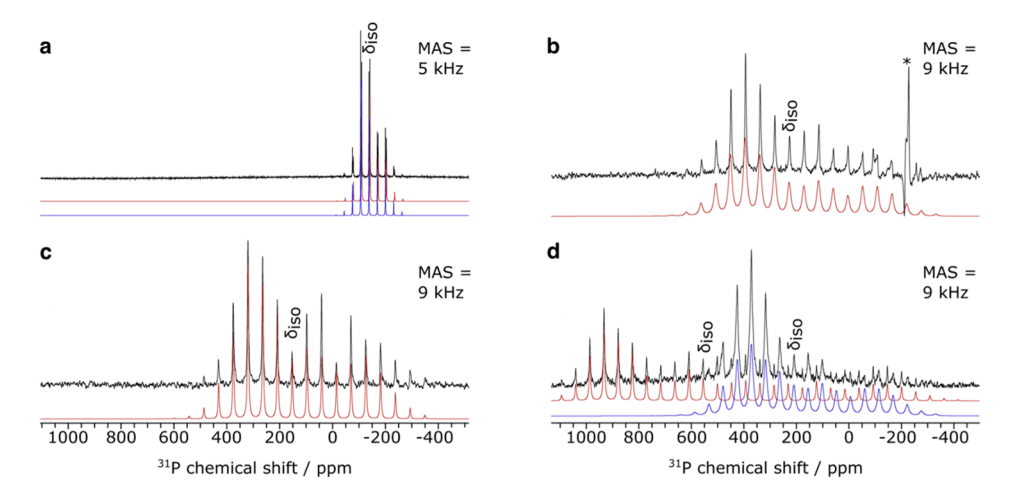


Figure 2. SS-MAS ³¹P NMR spectra for 1–4. (a) complex 1, MAS frequency = 5 kHz; (b) complex 2, MAS frequency = 9 kHz; (c) complex 3, MAS frequency = 9 kHz; (d) complex 4, MAS frequency = 9 kHz. Simulations (red and blue) are provided for the experimental data (black). The position of the isotropic peak is indicated (δ_{iso}) for each complex and a degradation product of 2 is highlighted by an asterisk (*). Note that there are two molecules in the asymmetric unit of 1 and that 4 has partially degraded into 2 during data acquisition.

Natural Localized Molecular Orbital (NLMO) approach has enabled elucidation of the underlying factors that determine the observed trends, including a remarkably large chemical shift anisotropy (CSA) for the bridging phosphido center in 4. This study has then permitted us to correlate the Th–P $\delta_{\rm iso}$ values to Mayer Bond Orders (MBOs), but we find that this is very dependent on the ancillary ligands. This highlights an important difference between N- and P-ligands, which is that the former tend to be the dominant component of the ligand field with ancillary ligands in a secondary role, whereas trends with the softer P-ligands are clearly much more ancillary ligand dependent.

■ RESULTS AND DISCUSSION

Experimental Solution ³¹P NMR Data. Compounds 1–4 were prepared as described previously. ^{52a} The purity and stability of 1–4 were checked and confirmed by examination of their ¹H, ¹³C{¹H}, ²⁹Si{¹H}, ³¹P, and ³¹P{¹H} NMR spectra recorded in C_6D_6 or D_8 -THF. As part of that process, regarding the ³¹P NMR data while the δ_{iso} values for 1 (–144.1 ppm) and 4 (553.5 ppm) were confirmed, ⁵² it was discovered that the originally reported δ_{iso} values for 2 (150.8 ppm) ^{52a} and 3 (24.5 ppm) ^{52a} are in fact 198.8 and 145.7 ppm, respectively. ^{32b} The original errors appear to be due to an isolated episode of referencing errors, but the δ_{iso} values for 1–4 of –144.1, 198.8, 145.7, and 553.5 ppm, Table 1 and Figures S1–S4, are now definitively confirmed by the solid-state magic angle spinning (SS-MAS) ³¹P NMR data (see below).

Experimental SS-MAS ³¹P **NMR Data.** To gain a fuller experimental characterization of the ³¹P chemical shift tensors in 1–4, ³¹P NMR spectra of powdered samples of 1–4 were collected with MAS frequencies of 5 kHz (1) and 9 kHz (2–4), Figure 2 and Table 1, which taken together with a natural abundance of 100% I=1/2 for the ³¹P nucleus provided satisfactory signal-to-noise ratios and hence reliable spectral simulations. The ³¹P SS NMR δ_{iso} values for 1–4 were determined to be -140.6/-137.1 (av. -138.9), 211.8, 151.8, and 554.8 ppm, respectively (with δ_{iso} values confirmed by also conducting the measurements with spinning frequencies of 2 (1) and 5 (2–4) kHz, Figure S5), which in each case are in good agreement (maximum $\Delta_{sol/ss} = 13$ ppm) with the

respective solution $\delta_{\rm iso}$ values given that precise $^{31}{\rm P}$ $\delta_{\rm iso}$ values are exquisitely sensitive to the chemical environment. Note for 1 the data quality permitted the extraction of two $\delta_{\rm iso}$ values in the spectral simulation, which results from there being two independent molecules of 1 in the crystallographic asymmetric unit that exhibit slightly different Th–P distances of 2.982(2) and 3.003(2) Å. 52a Since the Th–P bond length and $\delta_{\rm iso}$ values are rather similar we use the average SS-MAS $\delta_{\rm iso}$ for 1.

For 1, the average chemical shift tensor values δ_{11} , δ_{22} , and δ_{33} of -83.7, -102.3, and -233.1 ppm are fairly similar to one another, producing a relatively small chemical shift tensor span $(\Omega, \delta_{11} - \delta_{33})$ of 149.4 ppm, Figure 2a. The skew value $(\kappa, \delta_{11} - \delta_{33})$ $[3(\delta_{22}-\delta_{iso})]/\delta_{11}-\delta_{33}$) of 0.75 is between the values expected for axial (1.00) and terminal double bond (0.5),23 reflecting the Th-PH2 single bond linkage. In contrast, reflecting the presence of the Th=PH double bond, the corresponding δ_{11} , δ_{22} , δ_{33} , Ω , and κ values for **2** are 539.0, 368.6, -274.6, 813.6 ppm, and 0.58, Figure 2b, and this follows a similar pattern to that found for $[Ti(=PC_6H_2-2,4,6-Pr^i_3)(Me) \{(DippNCBu^{t})_{2}CH\}\}$ (Dipp = 2,6-diisopropylphenyl),⁷³ which has corresponding values of 630, 430, -400, 1030 ppm, and 0.61. The δ_{11} , δ_{22} , δ_{33} , Ω , and κ values of 441.3, 290.8, -279.1, 720.5 ppm, and 0.58 for 3, Figure 2c, are at first glance surprisingly similar to those for 2; however given the rather polar nature of Th-P bonds, this reflects the close relationship between a phosphinidene and phosphinidiide. On moving to 4 the presence of the bridging phosphide becomes apparent, with δ_{11} , δ_{22} , δ_{33} , Ω , and κ values of 1047.2, 972.0, – 357.2, 1404.4 ppm, and 0.89, Figure 2d. The presence of two large, positive chemical shift tensors and one negative one along with a κ value approaching the linear ideal underscores the axial nature of the Th=P=Th linkage. Notably, the Ω value for 4 is relatively large, 74 and while it is exceeded by terminal phosphido complexes such as $[W(\equiv P)]$ - $\{(Me_3SiNCH_2CH_2)_3N\}\}\ (\Omega = 2008 \text{ ppm}),^{75} [Mo(\equiv P)\{N-(3,5-Me_2C_6H_3)(Bu^t)\}_3] (\Omega = 2308 \text{ ppm}),^{76} [Mo(\equiv P)\{Me_2C_6H_3)(Bu^t)\}_3$ $(Ph)(Bu^t)_3$ ($\Omega = 2311 \text{ ppm}$), and $[Mo(\equiv P)$ - $\{(Me_3SiNCH_2CH_2)_3N\}\}$ ($\Omega = 2392 \text{ ppm}$), 75 it is, as far as we are aware, the largest recorded Ω value for a bridging phosphido ligand. Indeed, the ³¹P SS NMR data for 1-4

demonstrate a CSA Ω ordering of $(\mu - P)^{3-} > (=PH)^{2-} > (\mu - P)^{3-} > (\mu - P)^{3-} > (=PH)^{2-} > (\mu - P)^{3-} > (=PH)^{3-} >$ $PH)^{2-} > (-PH_2)^{1-}$.

We note that the δ_{33} values for 1-4 span the relatively narrow range of -233.1 to -357.2 ppm, though this is not surprising since the P-ligands have similar binding geometries. However, the larger variance for the δ_{11} and δ_{22} values for the different ligands implies that there are vacant orbitals of appropriate symmetry to couple with filled orbitals," and that the energy difference between these orbitals likely follows the trend 1 > 3 > 2 > 4. The greater interaction between these orbitals for 4 induces a large NMR deshielding and thus large δ_{11} (and δ_{22}). This is therefore investigated further with computational modeling (see below).

Computational Benchmarking of the ³¹P NMR Spectroscopic Properties of 1-4 and 1'-4'. With the solution and SS-MAS ³¹P NMR data on 1-4 confirmed we turned to the computational assessment of those data using Density Functional Theory (DFT, see Computational Details section for further details). Scalar Relativistic (SR) and twocomponent Spin-Orbit Relativistic (SOR) single point energy calculations for 1-4 were then acquired examining a range of functionals (BP86, SAOP, PBE0, and B3LYP, the latter two with a range of Hartree-Fock mixing), Tables S1-S4. Those data were then used to compute the SR and SOR 31 P NMR δ_{iso} values in benzene solvent continuums, converting calculated σ to δ values using the calculated σ_{iso} values for PH₃ in a benzene

It was determined that the B3LYP-HF50 SOR best reproduces the experimental ^{31}P δ_{iso} data for 1-4, Table 1. However, during the course of this study, it became apparent that memory limit issues for NBO and NLMO calculations prevented the NBO and NLMO data for 3 and 4 being computed. Since in that scenario changing the functional or basis sets was not appropriate due to large changes in computed $\delta_{\rm iso}$ values, we truncated the SiPri₃ substituents of the Tren^{TIPS} ligand in 1–4 to SiMe₃ (Tren^{TMS}), referred to as 1'-4', Figure 3; the Prⁱ Me groups were replaced by H atoms whose positions were optimized while keeping all the heavy atom positions fixed. The outcome of the truncation is that the computed SOR properties of 1' and 2' remain essentially unchanged on moving from 1 and 2, Tables S1 and S2. However, we note that the computed data for 3/3' and 4/4'

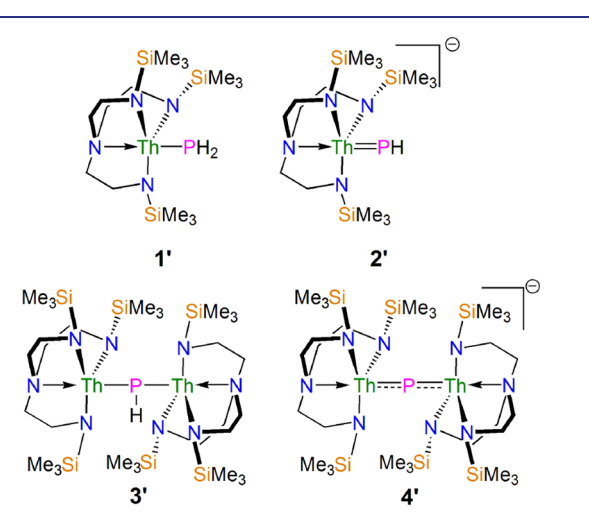


Figure 3. Truncated model complexes 1'-4' used for the MO, NBO, and NLMO analyses.

shift, Tables S3 and S4. For 3 good agreement was found (computed to within 4 ppm of experiment) but the computed 31 P chemical shift of 4 was computed to be \sim – 34 ppm relative to experiment; however, 4' is computed to within 3 ppm but then 3' is computed to be $\sim+20$ ppm from experiment. Considering the computational constraints and that the computed ³¹P δ_{iso} changes between 1-4 and 1'-4' are trivial when placed on the full δ_{iso} range of ³¹P chemical shifts, it was concluded that the truncated Tren TMS data of 1'-4' are most representative and practical to use, and so they are used in the analysis that follows. It should be noted, however, that given the sensitivity of 31 P δ_{iso} values to a wide range of parameters, it is remarkable how good the agreement of the calculated to experimental δ_{11} , δ_{22} , δ_{33} , Ω , and κ data are in terms of the breakdown for a given molecule, the consistently good agreement overall across all of 1'-4', and the fairly consistent parameters computed for 1-4 vs 1'-4'.

For 1' the SR calculation returns a ³¹P δ_{iso} value of -176.7 ppm, and this shifts to -149.9 ppm in the SOR calculation, the latter of which is in good agreement with the solution and SS $\delta_{\rm iso}$ values of -144.1 and -138.9 (av) ppm, respectively. The computed δ_{iso} value for 1' decomposes to δ_{11} , δ_{22} , δ_{33} , Ω , and κ values of -90.6, -148.5, -210.5, 119.9 ppm, and 0.04, in fair agreement with the experimental SS values of -83.7, -102.3, -233.1, 149.4 ppm, and 0.75, respectively. However, we note a significant divergence of the experimental and calculated δ_{22} and thus κ values for 1' ($\Delta \kappa_{\text{exp-calc}} = 0.71$), which likely reflects dynamic rotation of the PH2 group experimentally that is not captured by calculations on a static model. In passing, we note that a similar ¹⁵N NMR modeling averaging effect was found for the $-NH_2$ unit of $[Th(NH_2)\{N(SiMe_3)_2\}_3]^{30}$

The SR calculation for 2' gives a ³¹P δ_{iso} value of 191.3 ppm, and for the SOR calculation this moves to 209.0 ppm, which is between the solution and SS $\delta_{\rm iso}$ values of 198.8 and 211.8 ppm, respectively. The ~370 ppm shift to higher frequency for 2' compared to 1' can be seen to derive from δ_{11} , δ_{22} , and δ_{33} values of 511.8, 399.3, and -284.1 ppm, reflecting the Th=P double bond, resulting in a larger Ω value of 795.9 ppm and a κ value of 0.72, close to that expected for a terminal metalligand double bond. Overall, these values are in good agreement with those derived from the SS NMR data (539.0, 368.6, -274.6, 813.6 ppm, and 0.58, respectively).

The SR and SOR calculations for 3' afford δ_{iso} values of 40.7 and 167.5 ppm, respectively, the latter of which is in reasonable agreement with the experimental solution and SS $\delta_{
m iso}$ values of 145.7 and 151.8 ppm, respectively. However, the modeling of 3' is the poorest of 1'-4', and this can be understood when inspecting the computed δ_{11} , δ_{22} , δ_{33} , Ω , and κ values of 589.4, 160.4, −247.3, 836.7 ppm and 0.03 (cf. experimental values of 441.3, 290.8, -279.1, 720.5 ppm, and 0.58); while the δ_{33} value is reproduced well, both the δ_{11} and δ_{22} values are significantly over- and underestimated, which leads to the variation in the Ω value and the large discrepancy in the κ value. The same issue was found with the computed data for 3 as well as 3' suggesting that this is not a consequence of the Tren truncation, and given the finding for 1' and $[Th(NH_2) {N(SiMe_3)_2}_3]^{36}$ it is likely that experimentally there is dynamic rotation of the P–H group that does not render δ_{11} and δ_{22} completely equivalent—due to the threefold (or pseudo sixfold) rotation axis created by the Tren^{TIPS} ligands but which has the effect of reducing the difference between δ_{11} and δ_{22} experimentally whereas this effect is not captured by

Table 2. Computed Bond Orders, Charges, and NBO Data for 1'-4'a

	Mayer BI	Mayer BI Atomic charges			NBC	Th–P σ -component		NBO Th-P π-component				
Entry	Th-P	Th	P	%Th	%P	Th 7s/7p/6d/5f	P 32/3p	%Th	%P	Th 72/7p/6d/5f	P 3s/3p	
1'	0.63	2.12	-0.81	12	88	26/1/54/19	38/62	-	-	_	_	
2'	1.25	1.94	-1.22	16	84	14/0/64/22	41/59	17	83	0/0/75/25	0/100	
3′	0.71	2.05	-1.60	11	89	21/0/57/22	44/56	8	92	0/0/71/29	0/100	
				11	89	21/0/57/22	44/56	8	92	0/0/71/29	0/100	
4'	1.27	1.89	-1.25	14	86	18/0/62/20	50/50	16 ^b	84	0/0/70/30	0/100	
				14	86	18/0/62/20	50/50	16 ^b	84	0/0/70/30	0/100	

[&]quot;Calculations at the B3LYP-HF50 TZ2P all-electron ZORA spin-orbit (SOR) level in a benzene solvent continuum. "3-Center bond, the 16% is made up of $2 \times 8\%$ contributions from $2 \times Th$ atoms.

the calculations which represents the extreme static situation where the asymmetry of δ_{11} and δ_{22} would be exacerbated.

Lastly, for 4' the SR and SOR calculations return $\delta_{\rm iso}$ values of 387.3 and 551.1 ppm, respectively, where the latter is in very good agreement with the experimental solution and SS $\delta_{
m iso}$ values of 553.5 and 554.8 ppm, respectively. The axial Th= P=Th bonding environment in 4' is reflected in the computed δ_{11} , δ_{22} , δ_{33} , Ω , and κ values of 1033.6, 1011.3, -391.8, 1425.4 ppm, and 0.97, which is in good agreement with the experimental SS NMR data of 1047.2, 972.0, -357.2, 1404.4 ppm, and 0.89, respectively.

Molecular Orbital, Natural Bond Order, and Natural Localized Molecular Orbital Benchmarking of 1'-4'. Having established that the B3LYP-HF50 SOR calculations satisfactorily reproduce the key δ_{iso} , δ_{11} , δ_{22} , δ_{33} , Ω , and κ values for 1'-4', and hence 1-4, we reanalyzed their electronic structures at that level of theory, Table 2; previously the BP86 functional at the SR level was used to elucidate the electronic structures of 1-4, but we find that generally there is remarkably good agreement between the BP86 and B3LYP-HF50 models, and where there are significant differences this can be traced back to differences between NBO5 and NBO6, specifically cut-offs not returning components in the former that are included in the latter. In terms of MOs that are relevant to the following NMR discussion, we find (i) for 1' a Th-P σ -bond as the HOMO along with the P-lone pair as HOMO-4; (ii) for 2' Th=P π - (HOMO) and σ -bonds (HOMO-1) along with a P-lone pair (HOMO-5) that is the back-lobe of the P-H σ -bond; (iii) for 3' Th-P dative π -(HOMO) and covalent σ -bonds (HOMO-1) along with a Plone pair that is the back-lobe of the P-H σ -bond; (iv) for 4' Th=P two π - (HOMO and HOMO-1) and a σ -bond (HOMO-2). In all cases the Th-P bonds involve variable 3s and 3p contributions from P and predominantly 5f and 6d contributions from Th along with modest Th 7s contributions.

The Th-P MBOs for 1'-4' are computed to be 0.63, 1.25, 0.71, and 1.27. This reflects the polar covalent nature of these Th-P bonds, and that (i) the formal Th-P bond order doubles from 1' to 2'; (ii) in phosphinidiide 3' the Th-P bonds are formally single but supplemented with dative π bonding; (iii) that 4' has formally double (Lewis) and pseudotriple (MO) Th-P bonds that are bridging rather than terminal. The Th and P MDC_q charges for 1'-4' are 2.12/-0.81, 1.94/-1.22, 2.05/-1.60, and 1.89/-1.25. The variation in Th charge is reasonably small, but we note that the Th ion charges in 2' and 4' are lower than those in 1' and 3' reflecting the stronger donor power of terminal HP^{2-} and bridging P^{3-} compared to H_2P^{1-} and bridging HP^{2-} and also that bridging P³⁻ is a stronger donor than terminal HP²⁻. The P charges also reflect that pattern of charge donation from P to

Th. Overall, while there are some variations of the B3LYP data compared to the previous BP86 the agreement and trends remain good overall.

The MOs of 1'-4' that describe the Th-P interactions are clear-cut, but the MOs often contain minor intrusions of orbital coefficients from other atoms, most notably the Ndonors, so to provide a more localized and chemically intuitive model, we turned to NBO analyses. In general, though there are naturally variations between the previously reported BP86 and B3LYP-HF50 analysis presented here, the two sets of NBO data provide a consistent bonding picture in surprisingly good agreement with one another. In particular, the previously reported significant contributions of 7s character to the Th-P bonding, where Th bonding is generally thought to be dominated by 5f/6d character,8 is also consistently returned by the B3LYP NBO calculations as was the case for the prior BP86 calculations. In 1' the Th-P bond consists of 12% and 88% Th and P character, respectively. The Th component is 26/1/54/19% 7s/7p/6d/5f character, and the P part is 38/ 62% 3s/3p. The Th=P double bond in 2' is reflected in slightly larger Th contributions to the bonding, where the Th=P σ - and π -bonds are 16/84 and 17/83% Th/P character. The Th 7s/7p/6d/5f component of the Th=P σ -bond is 14/ 0/64/22% whereas for the π -bond it is 0/0/75/25%. The P 3s/3p contributions to the σ - and π -bonds are 41/59% and 0/ 100%, respectively. That the dianion charge of the $(HP)^{2-}$ unit in 3' is spread over two Th atoms but only one Th atom in 2' is reflected by the NBO data of 3'. Specifically, for 3' two Th-P bonds with Th/P character of 11/89% are found, and then the two dative Th–P π -bonds are each 8/92% Th/P character. In the Th-P σ -bonds the Th character is 21/0/57/22% 7s/ 7p/6d/5f character and the P component is 44/56% 3s/3p character. The Th character in the Th-P bonds is 0/0/71/29% 7s/7p/6d/5f, and the P is 0/100% 3s/3p. For 4' the Th=P σ -bonds and two π -bonds are 14/86 and 16/84% Th/P character, respectively. Note, the two π -bonds are represented as 3c2e bonds in the NBO analysis, and hence the Th/P character is a composite of 8/8/84% Th/Th/P character. Once again significant Th 7s contributions are found in the σ but not π -bonds, with Th 7s/7p/6d/5f contributions of 18/0/ 62/20 and 0/0/70/30%, respectively. For the P contributions, these are 3s/3p 50/50 and 0/100%, respectively.

In all instances, the Th-P bonding interactions described by the NBO calculations for 1'-4' exhibit electron occupancies of ≥1.82 electrons per orbital, and hence, the NBO orbitals are localized and thus the breakdowns are representative, especially as they are computed with a functional that reproduces the NMR parameters well. In order to further validate the NBO calculations and for the NLMO-NMR analysis below, we also performed the NLMO calculations,

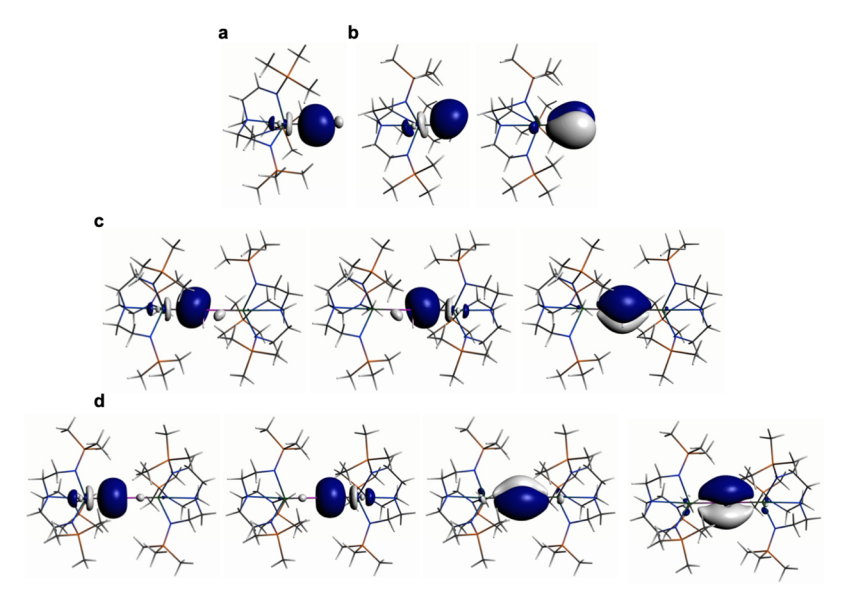


Figure 4. NLMO representations of: (a) the Th-P σ -bond in 1'; (b) the Th-P σ - and π -bonds in 2'; (c) the Th-P $2 \times \sigma$ - and $1 \times \pi$ -bond in 3'; (d) the $2 \times \sigma$ - and $2 \times \pi$ -bonds in 4'.

Figure 4 and Table S5. We find only relatively modest changes in the Th and P contributions to Th-P bonding between NBO and NLMO methods, giving confidence that this experimentally benchmarked analysis represents a quantification of the Th-P bonds in 1'-4' and hence 1-4.

Computational Shielding Analysis of 1'-4'. In order to develop the analysis of the nature of the Th-P bonds in 1-4, it is necessary to translate the chemical shift tensor $\delta_{\rm iso}$, δ_{11} , δ_{22} , δ_{33} , Ω , and κ parameters discussion to shielding, since chemical shifts derive from the nuclear shielding being adjusted with respect to the shielding and actual chemical shift of a reference (for this study with respect to PH3, itself referenced to the IUPAC standard of 85% H₃PO₄). Thus, the isotropic chemical shift $\delta_{\rm iso}$ derives from the isotropic shielding $(\sigma_{\rm iso})$, which in turn is composed of diamagnetic (σ^{d}) , paramagnetic (σ^{p}) , and spin-orbit (σ^{so}) shielding components. It naturally follows that δ_{11} , δ_{22} , and δ_{33} derive from σ_{11} , σ_{22} , and σ_{33} parameters,

Ramsey related σ_{iso} to σ^{d} and σ^{p} (eq 1).⁷⁸⁻⁸⁰ This does not map directly onto hybrid DFT (B3LYP); however when adjusted for σ^{so} , eq 2, this establishes a framework through which to rationalize NMR shielding calculations.⁸¹

$$\sigma_{\rm iso} = \sigma^{\rm d} + \sigma^{\rm p} \tag{1}$$

$$\sigma_{\rm iso} = \sigma^{\rm d} + \sigma^{\rm p} + \sigma^{\rm so} \tag{2}$$

The σ^d range for 1'-4' is 963.4-974.9 ppm, which is a relatively small variance. Even for the rather sensitive ³¹P nucleus this is to be expected because σ^{d} relates to tightly bound core electron density that responds little to perturbations in the valence region.⁸¹ Considering the large σ range (and hence δ range) of ³¹P NMR spectroscopy, a variance of 11.5 ppm can be considered to be negligible in terms of this discussion.

The σ^{so} values for $\mathbf{1}' - \mathbf{4}'$ show considerably more variance than the $\sigma^{\rm d}$ values. For 1'-4' the $\sigma^{\rm so}$ values are -14.7, -15.8, - 122.5, and -172.5 ppm. Recalling that the $\sigma_{\rm iso}$ values for 1'-4' are 494.4, 135.5, 177.0, and -206.5 ppm it is evident, given that $\sigma^{\rm d}$ shows little variance, that (i) $\sigma^{\rm so}$ is very similar for 1' and 2' yet their σ_{iso} values are different by ~359 ppm; (ii) σ^{so}

varies by ${\sim}107$ ppm from 2' to 3' but their $\sigma_{\rm iso}$ values are only ~42 ppm apart; (iii) σ^{so} from 3' to 4' varies by 50 ppm but the $\sigma_{\rm iso}$ shifts by ~384 ppm. Thus, while the $\sigma^{\rm so}$ values are significant and certainly cannot be isolated from the analysis they clearly are not the decisive factor in determining the overall $\sigma_{\rm iso}$ values. Indeed, we note that the $\sigma^{\rm so}$ values are $\sim 2-$ 15% of the $\sigma^p + \sigma^{so}$ values (vide infra). The similar σ^{so} values for 1' and 2' that significantly increase for 3' then 4' suggests increasingly efficient transfer of spin-orbit character to the NMR nucleus, P, from the Th ions. The NBO analysis revealed not only substantial Th s character in the Th-P bonds of 1'-4' but also large s contributions from the P centers, implying an efficient Fermi-contact pathway to transmit spin-orbit effects from Th to P by spin-dipole interactions. Spin-orbit effects are larger for 5f- than 6d-orbitals, and although the NBO analysis shows that the Th bonding is dominated by 6d contributions (51-78%) in each case, there are significant (19-30%) 5f-contributions. We note that the 5f-orbital contributions to the Th-P bonds are 19% and 22% for 1' and 2', then increase to 29% for 3', and then 30% for 4' which is also accompanied by the number and strength of Th-P interactions (i.e., single, double, single+dative, pseudotriple) increasing on going from 1' to 4', which is in-line with the increasing σ^{so} for $\mathbf{1}'$ to $\mathbf{4}'$.

$$\sigma^p \propto 1/r^3 \times \sum Q_{\text{ThP}}/\Delta E$$
 (3)

It is then logical to deduce that the σ^p component is likely the decisive factor for rationalizing the bonding in 1–4. The σ^p parameter can be represented in reduced form as per eq $3,^{37,48,78-81}$ where r is the radial expansion of the shielding electrons from the NMR nucleus (here ^{31}P), Q_{ThP} is the sum of the charge density and bond order matrix elements over the relevant atoms (here Th and P), and ΔE is the energy separation between the ground (filled) and excited (vacant) states in question. 22,78-80

The σ^p term is inversely proportional to the occupied-virtual orbital[s] energy gap[s] that become magnetically coupled in the presence of an externally applied magnetic field, so unusually small or large energy gaps would produce enhanced

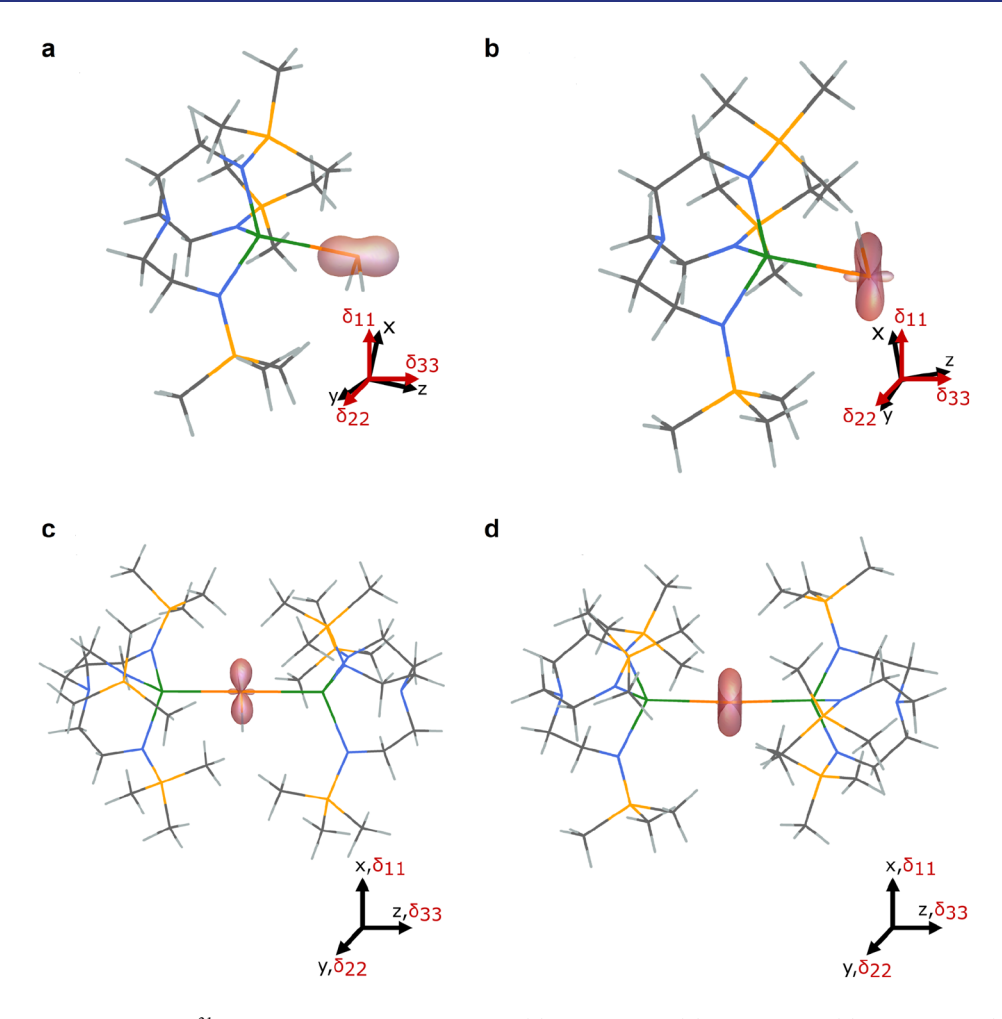


Figure 5. Plots of the δ_{11} , δ_{22} , and δ_{33} ³¹P tensor components for 1'-4'. (a) complex 1'; (b) complex 2'; (c) complex 3'; (d) complex 4'. The shielding surface is represented using the ovaloid convention where the distance from the P atom to a point on the surface is proportional to the chemical shift when the magnetic field is aligned along that direction in space. The shading of the surface denotes the sign of the shift where orange is positive and light orange is negative. The principal axes (x, y, z) are provided, along with the directions of the tensor components $(\delta_{11}, \delta_{22}, \delta_{33})$; note that for 3 and 4, these axes align fully.

or diminished magnetic coupling, respectively, and hence skew the analysis. Taking HOMO-LUMO gaps as indicative measures, the HOMO-LUMO gaps of 1'-4' are computed to be 4.2–5.9 eV, which suggests that any disproportionate effects on ΔE and hence σ^p for 1'-4' can be discounted.

Field-induced magnetic mixing of the ground state with lowlying, thermally inaccessible paramagnetic states, i.e. temperature independent paramagnetism (TIP), would result in ΣQ_{ThP} disproportionately distorting the values of σ^{P} . In order to exclude this, we examined the variable temperature magnetism of 1-4 using SQUID magnetometry over the temperature range 1.8-290 K (Figures S6 and S7). Complex 4 persistently returned a negative susceptibility, that is, a diamagnetic response. Complexes 1-3 exhibit very weak TIP, with values of 1.1166×10^{-4} , 3.3129×10^{-4} , and 2.4409 \times 10⁻⁵ cm³ mol⁻¹ K, similar to some U(VI) complexes, ^{29,37} with χT vs T linear regression R^2 values of 0.9970, 0.9995, and 0.9985, respectively, over the 85-290 K region. This suggests that any TIP effects are either absent (4) or negligible (1-3)and so the ΣQ_{Thp} term does not introduce a disproportionate effect on σ^p for 1–4.

Turning to the r^3 term, eq 3 shows that σ^p is inversely proportional to the cube of the radial expansion of the

shielding electrons from the NMR nucleus. This is because as the NMR nucleus (here ³¹P) has its charge withdrawn to the coordinated nucleus (here Th) this renders the NMR nucleus more electron deficient, and deshielded, and hence its valence orbitals contract reducing r and hence the $1/r^3$ term becomes larger. Thus, the larger the Th-P bond order the larger $1/r^3$ will be and hence the larger σ^p will be.⁴⁸ Taking all the above together, that the σ^p values for 1'-4' are computed to be -454.3, -817.9, -670.0, and -1008.9 ppm (and these dominant terms contribute to generating σ_{iso} values that in turn produce calculated $\delta_{\rm iso}$ values that match well to experimentally determined $\delta_{
m iso}$ values) is significant because it reflects the Th-P bonding environments of 1-4 of Th-P single bond, Th=P double bond, Th-P single bonds supplemented by dative π -bonds, and then Th-P pseudotriple (or in Lewis nomenclature Th=P double) bonds. Thus, the σ^{p} values of 1'-4' are in-line with the bonding motifs and MBOs of 1-4 in terms of the formal bond multiplicities of each respective Th-P linkage.

Shielding effects can be rationalized by using the rotated orbital model, $^{77,82-86}$ which describes the action of the angular momentum operator (L) on magnetically coupled occupied and virtual orbitals; this is intuitively visualized as a 90°

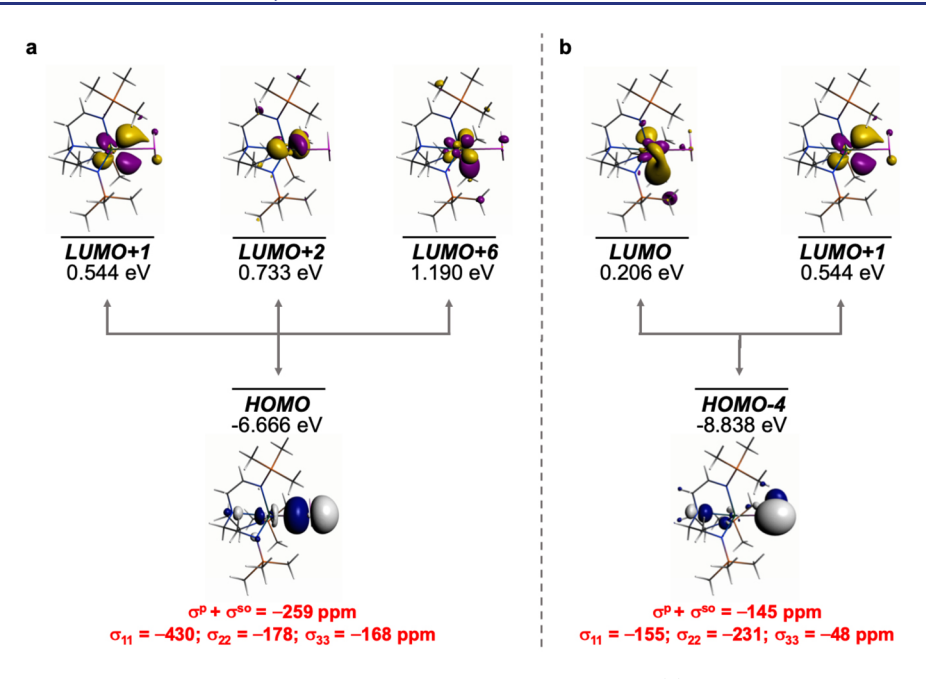


Figure 6. Dominant occupied and virtual MOs that contribute to the $\sigma_{\rm iso}$ and hence $\delta_{\rm iso}$ of 1'. (a) Magnetic coupling of the Th-P σ -bond with Th Sf/6d hybrids of pseudo π^* character. (b) Magnetic coupling of the P-lone pair with Th Sf/6d hybrids. The isotropic shielding values for the individual bonding components are given in red, and each is broken down into its principal component contributions.

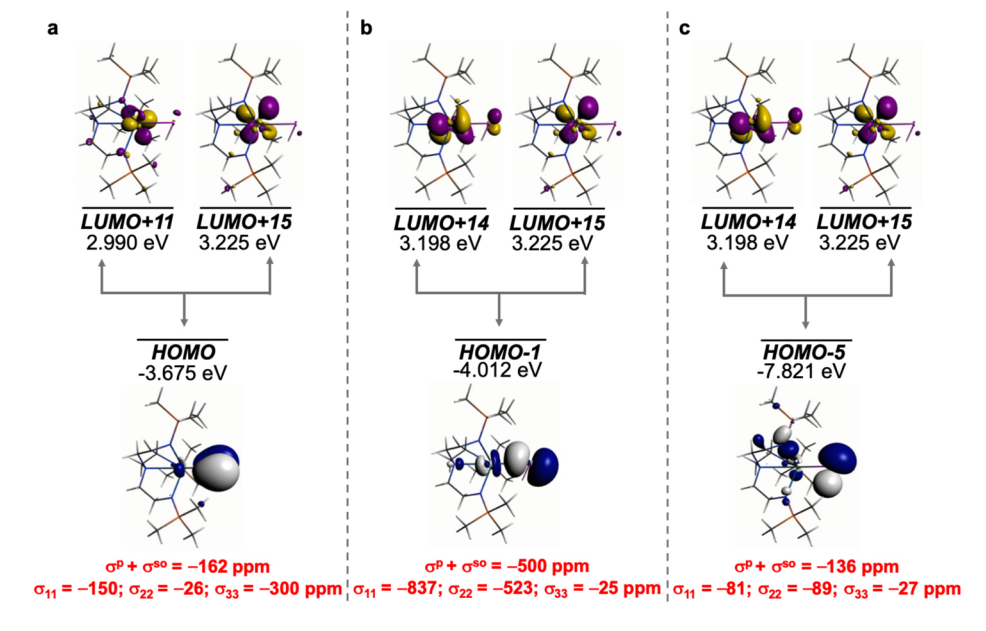


Figure 7. Dominant occupied and virtual MOs that contribute to the σ_{iso} and hence δ_{iso} of 2'. (a) Magnetic coupling of the Th–P π -bond with Th Sf/6d hybrids of pseudo π^* character. (b) Magnetic coupling of the Th–P σ -bond with Th=P π^* and Th Sd/6d orbitals. (c) Magnetic coupling of the P-lone pair with Th=P π^* and Th Sf/6d orbitals. The isotropic shielding values for the individual bonding components are given in red, and each is broken down into its principal component contributions.

rotation of an idealized occupied orbital to mix with a vacant orbital. The computed orientations of the 31 P σ_{11}, σ_{22} , and σ_{33} shielding tensor principal components are shown in Figure 5 (after conversion to $\delta_{11}, \ \delta_{22}$, and δ_{33} ; see Figure S8 for depictions in another set of orientations). As shown, these components align or almost align along the principal axes (x,y, and z), and for 2' and 3' one of the principal axes is almost parallel to the P–H bonds in each case. Thus, for 1'-4', in each case the occupied Th–P σ -orbital magnetically couples to virtual π^* Th–P orbitals via the action of the L_x or L_y angular momentum operators, which are perpendicular to the Th–P

bond that, by convention, lies along the z-direction of the principal axes (Figure 5). Consequently, this induces a paramagnetic term (a principal component of σ^p), perpendicular to the Th-P bond (z), along x or y. Since the P-H bonds are essentially perpendicular to the Th-P bonds in 1'-3', magnetic coupling of the Th-P occupied σ -orbital with virtual σ^* P-H orbitals can also contribute to deshielding perpendicular to the Th-P-H plane. Likewise, occupied Th-P π -orbitals can mix with virtual σ^* Th-P and P-H orbitals via the action of L_x and L_z , respectively.

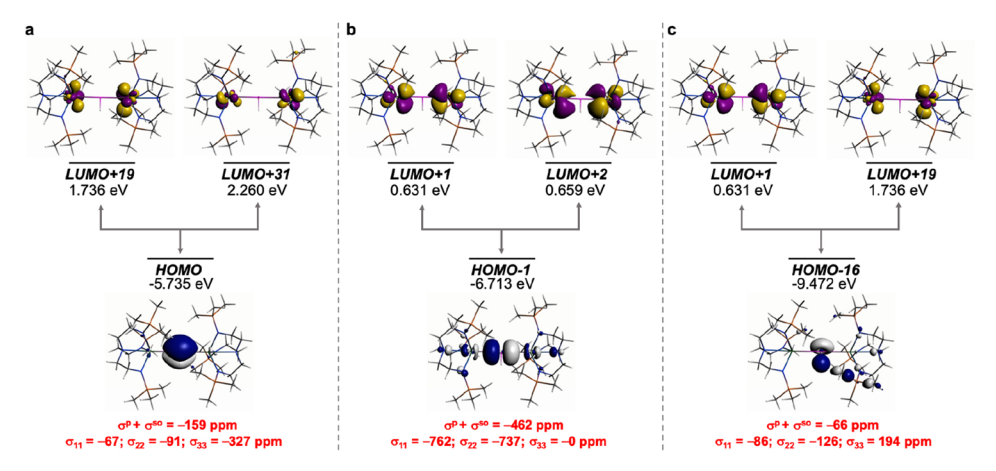


Figure 8. Dominant occupied and virtual MOs that contribute to the $\sigma_{\rm iso}$ and hence $\delta_{\rm iso}$ of 3'. (a) Magnetic coupling of the Th-P π -bond with Th = Ff/6d hybrids. (b) Magnetic coupling of the Th-P σ -bond with Th=P π^* and Th 6d orbitals. (c) Magnetic coupling of the P-lone pair with Th=P π^* and Th 6d orbitals. The isotropic shielding values for the individual bonding components are given in red, and each is broken down into its principal component contributions.

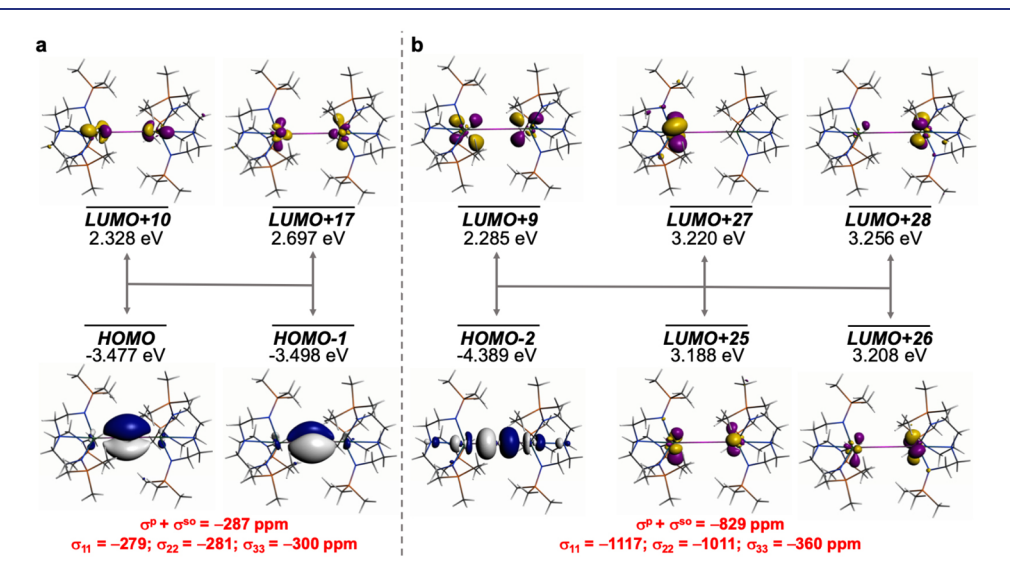


Figure 9. Dominant occupied and virtual MOs that contribute to the σ_{iso} and hence δ_{iso} of 4'. (a) Magnetic coupling of the two Th–P π -bonds with Th 5f/6d hybrids. (b) Magnetic coupling of the Th–P σ -bond with Th=P π^* and Th 5d/6d orbitals. The isotropic shielding values for the individual bonding components are given in red, and each is broken down into its principal component contributions.

Molecular Orbital Shielding Analysis of 1'-4'. MOs are often delocalized, and so their contributions to shielding can be distributed over numerous components, making them difficult to identify. Indeed, we note that the virtual MO manifolds of 1'-4' become increasingly densely packed and extensively delocalized resulting in some MO combinations becoming impossible to identify. However, the principal components that contribute to the $\sigma^p + \sigma^{so}$ terms of 1'-4'could be identified, thus permitting insight into the components that produce the observed $\delta_{\rm iso}$ values and hence the Th-P bonding in 1-4. The results of this analysis are presented in Figures 6-9, and where magnetic coupling combinations could be clearly identified they conform to the requirements that magnetic coupling of occupied and virtual orbitals must be symmetry allowed—since the angular momentum operators belong to the same irreducible representations as the rotational operators—and those rotationally orthogonal MO combinations should be spatially and energetically reasonably proximate.81

For 1', Figure 6, of the $\sigma^p + \sigma^{so}$ total of -469 ppm, -259 ppm is accounted for by field-induced magnetic coupling of the Th–P HOMO σ -bond with Th MOs of 6d- and 5f-parentage, one of which, LUMO+1, has the appearance of pseudo π^* -character. This is supplemented by magnetic coupling of the Th–P HOMO–4 P-lone pair with the LUMO and LUMO+1 accounting for another -145 ppm, resulting in a value of -404 of the -469 ppm being found by this method.

As anticipated, the analysis for 2' becomes more complicated than that of 1', Figure 7. The Th=P HOMO π -orbital magnetically couples with Th MOs of 6d- and 5f-character, the Th=P HOMO-1 σ -orbital magnetically couples with Th=P π^* and Th 5f/6d LUMOs +14 and +15, and additionally, the P-lone pair (HOMO-5) also magnetically couples with LUMOs +14 and +15. We note that the Th=P σ -bond is the dominant contributor (-500 ppm), followed by the π -bond (-162 ppm) and then P-lone pair (-136 ppm). Altogether these three components account for -798 of the -834 ppm for the σ^p + σ^{so} total for 2'.

Table 3. Natural Localized Molecular Orbital Contributions to the Principal ³¹P Nuclear Shielding Components ($\sigma^d + [\sigma^P + \sigma^{so}]$) of 1' and 2'a

Entry	NLMO	SR			SOR			$\Delta_{ m so}{}^d$				
•		\mathbf{L}^{b}	\mathbf{NL}^c	L+NL	\mathbf{L}^{b}	\mathbf{NL}^c	L+NL	\mathbf{L}^{b}	NL^c	L+NL	%NBO	Occ.
1'	Th-P oiso	-182	2	-180	-312	1	-311	-130	-1	-131	99.5	1.99
	σ_{11}	-266	2	-264	-440	1	-439	-174	-1	-175		
	σ_{22}	-216	2	-214	-428	2	-426	-212	0	-212		
	σ33	-64	2	-62	-68	2	-66	-4	0	-4		
	P-H σ_{iso}	-32	-2	-34	-22	-1	-23	10	1	11	98.4	1.97
	σ_{11}	22	-6	16	35	-10	25	13	-4	9		
	σ_{22}	-4	-31	-35	18	-22	-4	22	9	31		
	σ_{33}	-114	31	-83	-117	28	-89	-3	-3	-5		
	P-H σ_{iso}	-21	-2	-23	-13	-1	-14	8	1	9	98.1	1.96
	σ_{11}	57	-14	43	65	-14	51	8	0	8		
	σ_{22}	-19	13	-6	7	8	15	26	-5	21		
	σ_{33}	-101	-4	-105	-110	3	-107	- 9	7	-2		
	PLP_{iso}^{e}	-64	5	-59	29	4	33	93	-1	92	96.7	1.93
	σ_{11}	-138	9	-129	-8	9	1	130	0	130		
	σ_{22}	-24	1	-23	22	0	22	46	-1	45		
	σ_{33}	-29	4	-25	-20	5	-15	9	1	10		
	P 1s	515	0	515	533	0	533	18	0	18	100	2.00
	$P 2n^f$	295	5	300	286	1	287	-9	-4	-13	100	2.00
									_		00.1	1.00
2'	Th-P σ_{iso}	-289	-4	-293	-426	-9	-435	-137	-5	-142	99.1	1.98
	σ_{11}	-516	-1 -	-517	-682	-9	-691	-166	-8	-174		
	σ_{22}	-389	-7	-396	-605	-15	-620	-216	-8	-224		
	G 33	39	-5	-34	10	-4	6	-29	1	-28	00.2	1.05
	Th-P \(\pi_{iso}\)	-54	1	-53	-56	2	-54	-2	1	-1	98.3	1.97
	σ_{11}	-9	1	-8	4	1	5	13	0	13		
	σ_{22}	10	0	10	-11	0	-11	-21	0	-21		
	G 33	-163	4	-159	-160	4	-156	3	0	3	02.0	1.00
	P - H σ_{iso}	-4 7	-22	-69	-48	-22	-70	-1	0	-1	93.9	1.88
	σ_{11}	4	-3	1	- 7	-7	-14	-11	-4	-7		
	σ_{22}	-32	-69	-101	-28	-66	-94	4	3	7		
	σ ₃₃	-112	7	-105	-111	7	-104	1	0	1	07.6	1.05
	PLP_{iso}^{e}	-237	13	-224	-89 217	5	-84	148	-8	140	97.6	1.95
	σ_{11}	-392	20	-372	-217	11	-206	175	-9 12	166		
	σ_{22}	-307	16	-291	-70	4	-66	237	-12	225		
	σ ₃₃	-12	3	-9 51 4	20	1	21	32	-2	30	100	2.00
	P 1s P 2n ^f	514 274	$0 \\ 1$	514 275	534 265	0 1	534 266	20 -9	0	20	100 100	2.00 2.00
	r 2m	2/4	1	2/3	203		200	- 9	U	-9	100	2.00

^aB3LYP-HF50 TZ2P all-electron ZORA SR or SOR level in a benzene solvent continuum, all shielding parameters are in ppm. ^bLewis contribution of the NLMO. ^cNon-Lewis contribution of the NLMO. ^dDefined as $\sigma(SOR) - \sigma(SR)$ to isolate the SO component. ^eLone pair. ^f2s+2p orbitals.

Perhaps unsurprisingly the analysis for the phosphinidiide 3', Figure 8, is similar to the phosphinidene 2'. Specifically, the Th–P HOMO π -orbital magnetically couples with Th 6d-/5f-hybrids (LUMOs +19 and +31), the Th–P–Th HOMO–1 σ -linkage magnetically couples with pseudo π^* -/6d-character of the LUMOs +1 and +2, and the P-lone pair HOMO–16 orbital magnetically couples with LUMOs +1 and +19. Similarly to 2', these MO combinations follow a pattern of the Th–P σ -bond being the largest contributor (–462 ppm), followed by the π -bond (–159 ppm), and then the P-lone pair (–66 ppm). This totals a value of –687 of –793 ppm for the σ^p + σ^{so} total for 3'.

The removal of the proton from 3' to generate 4' is reflected in a MO shielding analysis that is distinct to 1'-3', Figure 9. The two Th–P π -bonds (HOMO and HOMO–1) magnetically couple with vacant Th 6d/5f hybrids (LUMOs +10 and +17) contributing –287 ppm, which is substantial but not double the Th=P π -contribution in 2' likely reflecting the bridging nature of the phosphido center in 4'. However, the Th–P HOMO–2 Th–P–Th σ linkage makes a significant contribution of –829 ppm, magnetically coupling to a variety

of virtual Th-P π^* -/6d- and 5f-/6d-orbital hybrids (LUMOs +9, +25 to +28). In total, the magnetic coupling of these MOs generates a total of -1116 ppm out of -1181 ppm for the σ^p + σ^{so} total for 4'.

What is clear from this analysis is that as the strength and multiplicity of the Th–P bonding interactions build up from 1 to 3 to 2 to 4, the $\sigma^p+\sigma^{so}$ totals likewise increase (cf. the $1/r^3$ argument above). Also, while there are clearly Th—P π -bonds present in 2 and 4 and that their contributions to the overall $\sigma^p+\sigma^{so}$ shieldings are not insignificant, the σ -bonds dominate the overall strength of the $\sigma^p+\sigma^{so}$ response in each case, which is then interleaved with the s-character of the Th and P bonding and the transmission of spin—orbit effects from Th to P which also reflects the 5f vs 6d contributions to the Th bonding.

As shown in Figures 6–9, the individual $\sigma^p + \sigma^{so}$ values for the Th–P σ , Th–P π , P–H σ , and P lone pair components of the Th–P bonding in 1'–4' can be broken down into their individual σ_{11} , σ_{22} , and σ_{33} values, providing some insight into the orbitals that principally contribute to the chemical shielding tensors. Figures 6–9 clearly indicate that large

Table 4. Natural Localized Molecular Orbital Contributions to the Principal ³¹P Nuclear Shielding Components ($\sigma^d + [\sigma^P + \sigma^{so}]$) of 3' and 4'^a

Entry	$NLMO^b$	SR				SOR						
		\mathbf{L}^c	\mathbf{NL}^d	L+NL	\mathbf{L}^{c}	\mathbf{NL}^d	L+NL	\mathbf{L}^{c}	Δ_{so}^e \mathbf{NL}^d	L+NL	%NBO	Occ.
3'	Th ₁ -P \sigma_{iso}	-211	-4	-215	-272	1	-271	-61	5	-56	98.1	1.96
	σ_{11}	-417	-13	-430	-496	-6	-502	-79	7	-72		
	σ_{22}	-216	-2	-218	-317	5	-312	-101	7	-94		
	σ_{33}	0	0	0	-4	2	-2	-4	2	-2		
	Th2-P oiso	-20 7	-4	-211	-266	0	-266	-59	4	-55	98	1.96
	σ_{11}	-411	-13	-424	-490	-6	-496	-79	7	-72		
	σ_{22}	-208	-3	-211	-302	4	-298	-94	7	-87		
	σ_{33}	0	0	0	-7	3	-4	-7	3	-4		
	Th-P Tiso	-120	16	-104	-113	15	-98	7	-1	6	91.1	1.82
	σ_{11}	-199	27	-172	-162	22	-140	37	-5	22		
	σ_{22}	7	1	8	-5	2	-3	-12	1	-11		
	σ_{33}	-169	21	-148	-172	21	-151	-3	0	-3		
	P - H σ_{iso}	-63	7	-56	-56	6	-50	7	-1	6	96.6	1.93
	σ_{11}	8	0	8	8	1	9	0	1	1		
	σ_{22}	-75	8	-67	-52	6	-46	23	-2	21		
	σ_{33}	-21	12	-109	-122	12	-110	-1	0	-1		
	P 1s	530	0	530	541	0	541	11	0	11	100	2.00
	P 2n ^f	303	-2	301	345	-2	343	42	0	42	100	2.00
4'	Th ₁ -P σ_{iso}	<i>–387</i>	-22	-409	-465	-15	-480	-78	7	-71	98	1.96
	σ_{11}	-593	-34	-627	-711	-23	-734	-118	11	107		
	σ_{22}	-585	-33	-618	-694	-23	-717	-109	10	99		
	σ_{33}	16	0	16	11	1	12	-5	1	-4		
	Th2-P \sigma_{iso}	-381	-21	-402	-457	-14	-471	-76	7	-69	98	1.96
	σ_{11}	-584	-32	-616	-692	-22	-714	-108	10	-98		
	σ_{22}	-576	-32	-608	-690	-21	-711	-114	11	-103		
	σ_{33}	16	0	16	11	1	12	-5	1	-4		
	Th1-P Tiso	-62	8	-54	-53	8	-4 5	9	0	9	94.4	1.87
	σ_{11}	-24	5	-19	-24	5	-19	0	0	0		
	σ_{22}	-46	7	-39	-25	5	-20	21	-2	19		
	σ_{33}	-115	14	-101	-112	13	-99	3	-1	2		
	Th2-P Tiso	-56	7	-49	-48	6	-42	8	-1	7	93.6	1.89
	σ_{11}	-24	5	-19	-23	4	-19	1	-1	0		
	σ_{22}	-20	3	-17	-20	3	-17	0	0	0		
	σ_{33}	-104	11	-93	-101	11	-90	3	0	3		
	P 1s	531	0	531	540	0	540	9	0	9	100	2.00
	$P 2n^f$	359	-2	357	339	- 2	337	-20	0	-20	100	2.00

^aB3LYP-HF50 TZ2P all-electron ZORA SR or SOR level in a benzene solvent continuum, all shielding parameters are in ppm. ^bThe Th₁ and Th₂ labels are used to distinguish the two slightly different sets of Th–P shielding data but the labeling is arbitrary. ^cLewis contribution of the NLMO. ^dNon-Lewis contribution of the NLMO. ^eDefined as $\sigma(SOR) - \sigma(SR)$ to isolate the SO component. ^f2s+2p orbitals.

deshielding in directions perpendicular to the Th–P bonds (z axis) is associated with the magnetic coupling of the occupied Th–P σ -bond with various virtual π^* -type orbitals. A larger number of low lying π^* -type orbitals are also associated with increased deshielding of the P nucleus. The rotated orbital model can provide significant insight when a common bonding motif with different substituents is examined, but here there are four different bonding motifs, and this combined with the complexity of the MO manifolds of 1'-4' renders some MO combinations impossible to identify. Due to the restrictions of the MO approach, we conducted a NLMO-NMR analysis since this provides a fuller picture.

Natural Localized Molecular Orbital Shielding Analysis of 1'-4'. The NLMO analysis of 1'-4' is compiled in Tables 3 and 4, and this methods describes Lewis and non-Lewis components of the bonding, 87,88 though we note that the analysis shows the non-Lewis components are minor with the Lewis components dominating the shielding. This is the case for SR and SOR models, which, by difference, permits the spin—orbit shielding effects to be determined. In each case, the

NLMOs are very similar to the corresponding NBOs, so since NLMOs are in essence NBOs that are expanded to achieve an orbital occupancy of 100% (2 electrons), by allowing other minor orbital coefficients to intrude, the NLMO analysis is valid.

The NLMO analysis reveals that the principal NLMOs involved in providing the relevant shielding for 1'-4' are, where present for a given molecule, the Th-P σ and π , P-H σ , P-lone pair, and core P orbitals (1s, 2s, 2p), which can be related back to the σ^p (Th-P) and σ^d (P-core) components of the MO shielding analysis. These NLMOs largely correlate to the corresponding NBOs, with percentage representations of \geq 91.1 and electron occupancies of \geq 1.87.

Focusing on the SOR data, for 1'-4' it is clear that the largest negative shielding component of each Th–P bond derives from the σ -components, with Lewis + non-Lewis totals being -311, -435, -537, and -951 ppm, respectively. The shielding response from the Th–P π -bonds is then smaller, being -54, -98, and -87 ppm for 2'-4', respectively. The P–H σ -bond contributions vary from -26 ppm for 1' to -70 ppm

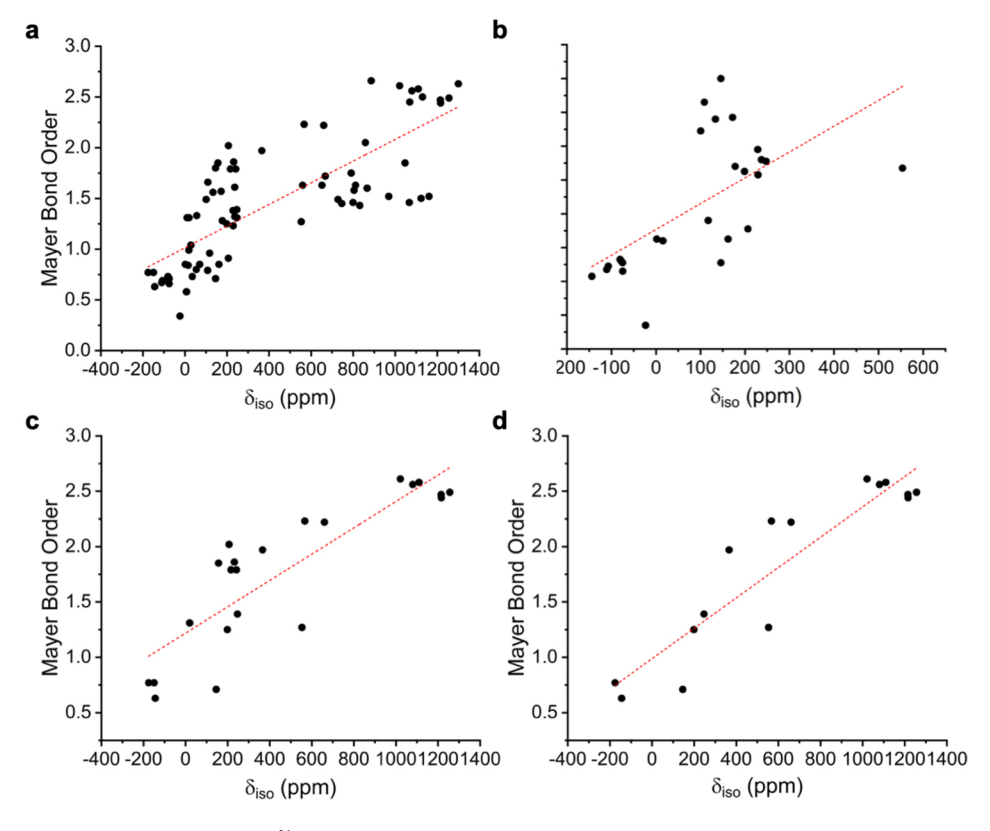


Figure 10. Correlations of experimental solution ³¹P NMR δ_{iso} data vs computed MBOs of representative metal P-ligand complexes, see Table S6 for the list of complexes. (a) Th and transition metal N-, Cp-, alkyl-, and aryloxide-ligands complexes 1–61, linear regression: MBO = (0.0011 × $\delta_{iso(exp)}$) + 1.0133, R² = 0.6122. (b) Th complexes 1–19 and 50, linear regression: MBO = (0.0015 × $\delta_{iso(exp)}$) + 0.9072, R² = 0.3860. (c) Th and transition metal N-ligand complexes 1–4, 22, 23–27, 31, 32, 36–42, 45, and 46, linear regression: MBO = (0.0011 × $\delta_{iso(exp)}$) + 1.2192, R² = 0.6861. (d) Th and transition metal amide-ligand complexes 1–4, 31, 32, 36–42, 45, and 46, linear regression: MBO = (0.0014 × $\delta_{iso(exp)}$) + 0.9881, R² = 0.8445.

for 2' to -50 ppm for 3'. Arrayed against these negative shielding parameters are the P-components, which are substantial for the 1s contributions alone, being 533, 534, 541, and 540 ppm for 1'-4'.

The $\Delta_{\rm so}$ data reveal that the Th–P σ -bonds are most greatly affected by spin–orbit effects but the Th–P π -bonds are far less affected. This can be related back to the bonding analysis, which showed substantial P s-character in the Th–P σ -bonds, but virtually exclusive P p-character in the Th–P π -bonds. Thus, the presence of s-character permits spin-polar transmission of spin–orbit effects, but this is greatly reduced in the π -bonds. The P-lone pairs contain s-character, and notably, the $\Delta_{\rm so}$ data reveal that they too exhibit large spin–orbit effects, whereas unsurprisingly, the core P orbitals are little affected by spin–orbit effects. Overall, these data are in agreement with the MO analysis and confirm that the $\delta_{\rm iso}$ and hence shielding properties of the Th–P linkages in 1'–4' are overwhelmingly dependent on the Th and P atoms with minor contributions from the P–H bonds where present.

Noting that the $\delta_{\rm iso}$ and hence shielding properties of the Th–P linkages in 1'-4' are dependent on the Th and P atoms it is then instructive to examine the NLMO breakdown of each $(\sigma^{\rm d} + [\sigma^{\rm p} + \sigma^{\rm so}])$ component of the Th–P bonds. The NLMO analysis does not explicitly identify the localized vacant orbitals that are magnetically coupled to the occupied orbitals, but using the MO shielding analysis above as a guide, the individual σ_{11} , σ_{22} , and σ_{33} values from the NLMO analysis

can be inspected and rationalized; it is intuitively most straightforward to start with the axially symmetric 4'.

For 4', Table 4, both Th–P σ -bonds (in reality the 3c2e Th–P–Th P 3p NBO interactions expressed as separate combinations in the NLMO framework) are aligned along the principal z-axis, and exhibit large σ_{11} and σ_{22} deshieldings that can be visualized as resulting from 90° rotation of those P 3p-orbitals into the y and x directions; this is the magnetic coupling of σ and π^* Th–P bonds by the action of L_x and L_y , respectively. The two Th–P π -bond P-orbitals are each aligned along the principal x and y axes, and each exhibits a large σ_{33} deshielding (along z), which is due to the magnetic coupling of these occupied orbitals with virtual π^* -orbitals via the action of L_z .

The presence of the P–H H atom in 3' results in an asymmetry of the bonding at P which can be clearly seen in the NLMO data, Table 4. The two Th–P σ -bonds (again, in reality the 3c2e Th–P–Th P 3p NBO interaction expressed as separate combinations in the NLMO framework) are aligned along the principal z-axis. Their σ_{11} and σ_{22} ³¹P deshielding values contain contributions owing to the magnetic coupling of the occupied Th–P σ -orbital with virtual π^* -type orbitals via the action of L_x and L_y . However, unlike for 4', σ_{11} and σ_{22} are now no longer approximately equal, with each exhibiting a larger value (av. –499 ppm) and a smaller value (av. –305 ppm); this asymmetry results from the P–H σ -bond being aligned along the same axis as σ_{11} and the Th–P dative π -symmetry "lone pair" residing along the same axis as σ_{22} . This

can likewise be seen in the data for those two linkages, each of which contains a large σ_{33} deshielding that results from magnetic coupling of the P–H or P π 3p-orbitals from the principal x- and y-axes with the π^* - and P–H σ^* -vacant orbitals via the action of L_z . Interestingly, the Th–P π -bond P 3p-orbital exhibits a significantly deshielded σ_{11} value, which is due to the magnetic coupling of this orbital with the Th–P σ^* orbital (action of L_x), but the corresponding σ_{22} deshielding value for the P–H σ -linkage due to magnetic coupling with the Th–P σ^* orbital is far smaller.

For 2', the Th-P bond is aligned along the principal z-axis, and hence it exhibits large σ_{11} and σ_{22} deshielding values; the former results from rotation of the Th–P σ -bond into the Th– P π^* orbital by the action of L_x and the latter results from orthogonal Th-P σ - π * magnetic coupling by the action of L_v . The Th–P π -bond is aligned with the σ_{22} principal component, and it exhibits a large σ_{33} deshielding value that results from $\pi - \sigma^*(P-H)/\pi^*(Th-P)$ magnetic coupling by the action of L_z . The P-H bond is only slightly off the same axis as σ_{11} , which is reflected by large σ_{22} and σ_{33} deshielding values that stem from magnetic coupling of the associated P 3p orbital with σ^* (Th-P) and π^* (Th-P) virtual orbitals, respectively, by the action of L_v and L_z . The P lone pair is almost aligned with the direction of the σ_{33} principal component (and hence z axis), but deviates sufficiently for its σ_{11} and σ_{22} deshielding values to be rather different, and this is magnetic coupling of the P lone pair with the P-H π^* (σ_{11}) and σ^* (σ_{22}) bonds by the action of L_x and L_y .

Lastly, for $\mathbf{1}'$ again the Th-P σ -bond is aligned along the principal z-axis (and the direction of the σ_{33} principal component), which is reflected in its σ_{11} and σ_{22} deshielding values being substantial via the action of L_x and L_y . However, the two P-H bonds and P-lone pair are in between the principal x- and y-axes (and are not aligned with the directions of σ_{11} or σ_{22}), which makes their σ_{11} and σ_{22} shielding data relatively uninformative, but the effect on σ_{33} of magnetic coupling of the P-H orbitals with Th-P π^* -orbitals by the action of L_z is clear. Nevertheless, it is evident from the NLMO data that it is the Th-P σ -bond that is most important in determining the δ_{iso} value of $\mathbf{1}'$.

Correlating ³¹P NMR Spectroscopic Chemical Shift to Metal–Phosphorus Bond Order. With the bonding and shielding properties of 1'-4', and hence 1-4 determined, quantified, and rationalized, we sought to correlate the observed $\delta_{\rm iso}$ values to the metal–phosphorus bond orders. We surveyed the literature and selected a range of representative compounds that were structurally characterized, have clear ³¹P NMR data, and cover the range of dative single bond phosphines, covalent single bond phosphanides, covalent double bond phosphinidenes, and covalent triple bond phosphidos. In addition to 1-4, this adds an additional 57 complexes to the analysis, spanning Th, Sc, Ti, Zr, Nb, Mo, W, Re, Ru, Os, Co, Rh, Ir, and Ni metals, all computed at the same B3LYP level as 1-4, Table S6. $^{50-56,59,60,67,70,73,75,76,85,89-117}$ We thus plotted $\delta_{\rm iso}$ values vs computed MBOs for a wide

We thus plotted δ_{iso} values vs computed MBOs for a wide range of Th and groups 3–10 of the transition metals, Figure 10.

The plot of all compounds, Figure 10a, shows a general trend of increasing MBO with increasing $\delta_{\rm iso}$, and hence increased deshielding, which as suggested by the analysis above will be most dependent on the $\sigma^{\rm p}$ property. However, linear regression shows the correlation to be $R^2 = 0.6122$. It should be noted that this collection of compounds has a very wide

range of ancillary ligands, where no trend is discernible in terms of ancillary ligand variations, and also as evidenced by the analysis of 1-4 and 1'-4' $\sigma^{\rm so}$ is variable which will skew the results compared to an analysis based on σ^p alone. This contrasts to the situation we recently reported for amine, amide, imido, and nitride analogues,³⁷ where those ligands are the strongest donors and so other ligands are very much in a secondary ancillary role and hence the R^2 correlation is much better even for a wide range of coligands. Nevertheless, when considering all compounds examined in terms of the coordinated P-ligand, some clear trends emerge. This divides Figure 10a into four quadrants, as follows: (i) "top left" (MBO > ~1.25; δ_{iso} < 500 ppm) early metal terminal phosphinidenes; (ii) "top right" (MBO > ~1.5; δ_{iso} > 500 ppm) early metal terminal phosphidos; (iii) "bottom left" (MBO < ~1; $\delta_{\rm iso}$ < 500 ppm) bridging phosphinidiides and M-P single bonds; (iv) "bottom right" (MBO ~ 1.2–1.7; δ_{iso} > 500 ppm) late dblock terminal phosphinidenes. Thus, in general, compounds with the most well-developed M-P multiple bonds that will exhibit the most covalency tend to sit above the dotted red least-squares fit line in Figure 10a, whereas those that are more polarized, or are bonded to electron-rich metals where population of antibonding orbitals may be becoming a factor, sit below the line. The results here for P-ligands suggests that P-complexes are much more varied as a consequence of the ancillary ligands, which reflects the relative hardness of N vs P in HSAB theory, that is the P-ligand environments are more sensitive to other ligands. To probe this hypothesis further we analyzed the data in more depth.

Figure 10b shows a plot of all of the Th complexes examined in this study. The $R^2 = 0.3860$ is worse than the plot of all complexes. This reflects the wide range of ancillary ligands and also that with even greater numbers of compounds, metals, and ligands, averaging effects occur. This suggests that the ancillary ligands indeed play a significant role in determining how electrophilic the Th ions will be, hence directly modulating the Th-P bonds in question, which will then directly impact on the σ and then δ properties. When the scope of ancillary ligands is narrowed down to N-donor ligands, Figure 10c, the R^2 value improves markedly to 0.6861, which supports the arguments presented above about ancillary ligand effects. Indeed, when the range of ancillary ligand types is narrowed further to only amides, Figure 10d, then $R^2 = 0.8445$. Thus, the conclusion is clear, while modeling hard nitrides, imides, and amides can largely be done irrespective of the nature of any other ancillary ligands; because phosphorus is softer than nitrogen when the same analysis is applied to M-P complexes, the correlation is not as good because the ancillary ligands are not secondary but also effectively also primary drivers of $\sigma_{\rm iso}$ and hence δ_{iso} . We thus conclude that when investigating the covalency of M-P bonds by ³¹P NMR spectroscopy it is necessary to bound correlations within the same family of ancillary ligands, whereas this is not necessary for M-N bonds. Nevertheless, the correlation equations provided in Figure 10 may form the basis for qualitative general assessments of $\delta_{\rm iso}$ versus MBOs across all ligand types and may be regarded as more quantitative for amide ancillary ligand complexes.

SUMMARY AND CONCLUSIONS

In summary, we have examined the solution and SS ³¹P NMR spectroscopy of a family of four Th complexes which exhibit Th-PH₂, Th=PH, Th-P(H)-Th, and Th=P=Th linkages in 1-4. Through modeling of SS data and computational

analysis the $\delta_{\rm iso}$ values have been decomposed into their constituent chemical shift tensors giving information about the chemical shift anisotropies of the P-environments in 1–4 and revealing a record CSA for a bridging phosphido center. The $^{31}{\rm P}$ SS NMR data for 1–4 demonstrate a CSA ordering of (μ -P) $^{3-}$ > (=PH) $^{2-}$ > (μ -PH) $^{2-}$ > (-PH $_2$) $^{1-}$. Thus, this work has introduced $^{31}{\rm P}$ NMR spectroscopy for quantitative determination of metal–ligand covalency in f-element chemistry.

Inspection of the $\sigma_{\rm iso}$ data has enabled dissection into $\sigma^{\rm d}$, $\sigma^{\rm p}$, and $\sigma^{\rm so}$ contributions, revealing invariant $\sigma^{\rm d}$, but highly variable $\sigma^{\rm p}$ and $\sigma^{\rm so}$. This reflects the Th–P bond multiplicities and also the amount of s-character in the Th–P bonds that permits transmission of spin–orbit effects from Th to P by spin-polar effects. Shielding analysis has revealed the nature of the MOs that contribute to the $\sigma_{\rm iso}$, and hence $\delta_{\rm iso}$, values by magnetic coupling of filled and orthogonal virtual orbitals where in each case the P $\delta_{\rm iso}$ value is virtually exclusively due to the nature of the Th–P bonds. It is clear that the Th–P σ -bonds dominate over the σ tensors, as these are the most affected by spin orbit effects, but the π -bond contributions are not insignificant.

By experimentally benchmarking the data, the nature of the Th–P bonding has been quantified by NBO and NLMO methods, and it is interesting to note that although there are variations between experimentally benchmarked B3LYP-HF50-SOR and model BP86 calculations the data are remarkably similar between the two functionals, which confirms the unusual quite significant 7s contributions to the Th–P bonds of 1–4 where normally 6d/5f-orbital character (and 6d > Sf) is the dominant feature of Th chemical bonding. This suggests that BP86 is quite appropriate for computing coarse parameters, e.g., orbital % contributions and bond orders, but B3LYP is needed for detailed calculation of heavily spin–orbit dependent parameters like $\delta_{\rm iso}$.

This study has permitted us to correlate the Th-P δ_{iso} values to MBOs over a wide range of metals spanning the early, mid, and late d-block in addition to Th. However, we find that the correlation is very much dependent on the ancillary ligands, highlighting an important difference between N- and P-ligands, which is that N-ligands tend to be the dominant component of the ligand field with ancillary ligands in a secondary role, whereas trends with the softer P-ligands are clearly much more ancillary ligand dependent. We thus conclude that when investigating the covalency of M-P bonds by ³¹P NMR spectroscopy, it is necessary to bound correlations within a given family of ancillary ligands, whereas this is not necessary for M-N bonds. Nonetheless, the correlation equations provided in this work may form the basis for qualitative initial assessments of $\delta_{
m iso}$ versus MBOs across all ligand types and may be regarded as more quantitative for amide ancillary ligand complexes.

■ EXPERIMENTAL SECTION

Experimental Details. The compounds $[Th(PH_2)(Tren^{TIPS})]$ (1, $Tren^{TIPS} = \{N(CH_2CH_2NSiPr_{3}^i)_3\}^{3-}$), $[Th(PH)(Tren^{TIPS})][Na-(12C4)_2]$ (2, 12C4 = 12-crown-4 ether), $[\{Th(Tren^{TIPS})\}_2(\mu\text{-PH})]$ (3), and $[\{Th(Tren^{TIPS})\}_2(\mu\text{-P})][Na(12C4)_2]$ (4) were prepared as described previously. Sea The formulations and purity were confirmed by 1H , $^{13}C\{^1H\}$, $^{29}Si\{^1H\}$, ^{31}P , and $^{31}P\{^1H\}$ NMR spectra recorded in C_6D_6 or D_8 -THF; those spectra are essentially the same as the originals, but given the identified ^{31}P δ_{iso} issue for 2 and 3 all ^{31}P NMR spectra are provided in the Supporting Information.

Solution ¹H, ¹³C(¹H), ²⁹Si(¹H), and ³¹P(¹H) NMR spectra were recorded on a Bruker AV III HD spectrometer operating at 400.07,

100.60, 79.48, and 161.95 MHz, respectively; chemical shifts are quoted in ppm and are relative to TMS (1H, 13C, and 29Si) and 85% H₃PO₄ (³¹P), respectively. Solid-state direct excitation ³¹P NMR spectra were recorded by using a Bruker 9.4 T (400 MHz ¹H Larmor frequency) AVANCE III spectrometer equipped with a 4 mm HFXY MAS probe. Experiments were acquired at ambient temperature using various MAS frequencies. Samples were packed into 4 mm o.d. zirconia rotors in a glovebox, and sealed with a Kel-F rotor cap. The ^{31}P ($\pi/2$)-pulse duration was 4 μ s, and a Hahn-echo $au_{
m r} - \pi - au_{
m r}$ sequence of 2 rotor periods total duration was applied to ³¹P after the initial $(\pi/2)$ -pulse to circumvent receiver dead-time. The signal was acquired for ~10 ms and between 128 and 3744 transients were coadded, with repetition delays of 3.2 s. Magnitude phase correction was used for the ³¹P MAS NMR spectrum of 4 owing to the large spectral range of the spinning side bands. The degradation product of 2 exhibits an antiphase ³¹P NMR peak, likely due to evolution of the J_{PH} coupling under the employed echo. Spectral simulations were performed in the solid line-shape analysis (SOLA) module v2.2.4 in Bruker TopSpin v4.0.9. The ³¹P chemical shifts were referenced to 85% H₃PO₄ externally using ammonium dihydrogen phosphate (0.8 ppm). Care must be taken with air sensitive compounds to minimize sample decomposition during measurements, and due consideration must be given to if data are robust if any minor decomposition occurs. Static variable-temperature magnetic moment data were recorded in an applied dc field of 0.1 T on a Quantum Design MPMS 3 superconducting quantum interference device (SQUID) magnetometer by using recrystallized powdered samples. Care was taken to ensure complete thermalization of the sample before each data point was measured, and samples were immobilized in an eicosane matrix to prevent sample reorientation during measurements. Diamagnetic corrections were applied using tabulated Pascal constants, and measurements were corrected for the effect of the blank sample holders (flame-sealed Wilmad NMR tube and straw) and eicosane

Computational Details. Restricted calculations were performed using the Amsterdam Density Functional (ADF) suite version 2017 with standard convergence criteria. ^{118,119} Geometry optimizations were performed using coordinates derived from the respective crystal structures as the starting points and were either the full models 1-4 (for 1 with two molecules in the asymmetric unit we used the molecule with the Th-P distance of 2.9817 Å) with the noncoordinating cation components in 2 and 4 removed or the analogous truncated models $1'-\bar{4}'$. Analogously, for the correlation study published crystallographic coordinates were used as the starting point for calculations on 5-50 (with any noncoordinating ions removed from the models). The H atom positions were optimized, but the non-H atom positions were constrained as a block. The DFT geometry optimizations employed Slater type orbital (STO) TZ2P polarization all-electron basis sets (from the Dirac and ZORA/TZ2P databases of the ADF suite). Scalar relativistic (SR) approaches (spin-orbit neglected) were used within the ZORA Hamiltonian 120-122 for the inclusion of relativistic effects, and the local density approximation (LDA) with the correlation potential due to Vosko et al. was used in all of the calculations. ¹²³ Generalized gradient approximation corrections were performed using the functionals of Becke and Perdew. 124,125 See the Supporting Information for final coordinates and energies, Tables S7-\$71.

SR and two-component spin—orbit relativistic (SOR) ZORA TZ2P polarization all-electron single point energy calculations were then run on the geometry optimized coordinates. The conductor-like screening model (COSMO) was used to simulate solvent effects. The functionals screened included BP86, SAOP, B3LYP-HFXX (XX = 20 (default in ADF), 30, 40, and 50%), and PBE0-HFXX (XX = 25 (default in ADF) and 40%). Overall, the B3LYP-HF50 functional gave the closest agreement of computed NMR properties compared to experiment, so it was selected for further in-depth study. MDC_q charges and MBOs were computed within the ADF program.

NBO and NLMO analyses were carried out using NBO6. 126 The MOs, NBOs, and NLMOs were visualized by using ADFView.

NMR shielding calculations were carried out using the NMR program within ADF. $^{87,88,127-131}$ Calculated nuclear shieldings were converted to chemical shifts by subtraction from the calculated nuclear shielding of PH $_3$ calculated at the same level (SR $\sigma_{\rm iso}=571.7;$ SOR $\sigma_{\rm iso}=584.5$ ppm) and correcting for PH $_3$ $\delta_{\rm iso}=-240$ ppm with respect to 85% H $_3$ PO $_4$. $^{132-134}$ MO contributions to the nuclear shieldings were calculated at the scalar and two-component spin—orbit levels, the former with the FAKESO key. Scalar and two-component spin—orbit NLMO-NMR calculations of the computed nuclear shieldings were carried out using NBO6 and ADF. These calculations used the Hartree–Fock RI scheme to suspend the dependency key and avoid numerical issues. Shielding tensors (converted to chemical shift tensors) were visualized using Tensor-View. 135

ASSOCIATED CONTENT

Data Availability Statement

Data are provided in the Supporting Information or are available from the authors upon reasonable request.

Supporting Information

The Supporting Information is available free of charge at https://pubs.acs.org/doi/10.1021/jacs.3c02775.

Additional experimental and computational data associated with this manuscript (PDF)

AUTHOR INFORMATION

Corresponding Authors

Ralph W. Adams — Department of Chemistry, The University of Manchester, Manchester M13 9PL, U.K.; orcid.org/0000-0001-8009-5334; Email: ralph.adams@manchester.ac.uk

Daniel Lee — Department of Chemical Engineering, The University of Manchester, Manchester M13 9PL, U.K.; orcid.org/0000-0002-1015-0980; Email: daniel.lee@manchester.ac.uk

Stephen T. Liddle — Department of Chemistry, The University of Manchester, Manchester M13 9PL, U.K.; ⊚ orcid.org/ 0000-0001-9911-8778; Email: steve.liddle@ manchester.ac.uk

Authors

Jingzhen Du − Department of Chemistry, The University of Manchester, Manchester M13 9PL, U.K.; ocid.org/0000-0003-4037-9281

Joseph Hurd — Department of Chemical Engineering, The University of Manchester, Manchester M13 9PL, U.K.

John A. Seed – Department of Chemistry, The University of Manchester, Manchester M13 9PL, U.K.; ocid.org/0000-0002-3751-0325

Gábor Balázs – Institute of Inorganic Chemistry, University of Regensburg, 93053 Regensburg, Germany

Manfred Scheer – Institute of Inorganic Chemistry, University of Regensburg, 93053 Regensburg, Germany

Complete contact information is available at: https://pubs.acs.org/10.1021/jacs.3c02775

Notes

The authors declare no competing financial interest.

ACKNOWLEDGMENTS

Funding and support from the UK Engineering and Physical Sciences Research Council (EPSRC, grants EP/F030517/1, EP/M027015/1, EP/S033181/1, EP/V007580/1, EP/

W021463/1), European Research Council (grants 239621 and 612724), the EPSRC UK National Electron Paramagnetic Resonance Facility for access to SQUID magnetometry, and The University of Manchester including computational resources and associated support services from the Computational Shared Facility are gratefully acknowledged. The Alexander von Humboldt Foundation is thanked for a Friedrich Wilhelm Bessel Research Award to S.T.L.

REFERENCES

- (1) Choppin, G. R. Covalency in f-Element Bonds. *J. Alloys Compd.* **2002**, 344, 55–59.
- (2) Kaltsoyannis, N. Does Covalency Increase or Decrease across the Actinide Series? Implications for Minor Actinide Partitioning. *Inorg. Chem.* **2013**, 52, 3407–3413.
- (3) Neidig, M. L.; Clark, D. L.; Martin, R. L. Covalency in f-Element Complexes. *Coord. Chem. Rev.* **2013**, 257, 394–406.
- (4) Hayton, T. W. Metal-Ligand Multiple Bonding in Uranium: Structure and Reactivity. *Dalton Trans.* **2010**, *39*, 1145–1158.
- (5) Jones, M. B.; Gaunt, A. J. Recent Developments in Synthesis and Structural Chemistry of Nonaqueous Actinide Complexes. *Chem. Rev.* **2013**, *113*, 1137–1198.
- (6) Hayton, T. W. Recent Developments in Actinide-Ligand Multiple Bonding. *Chem. Commun.* **2013**, 49, 2956–2973.
- (7) La Pierre, H. S.; Meyer, K. Activation of Small Molecules by Molecular Uranium Complexes. *Prog. Inorg. Chem.* **2014**, *58*, 303–415
- (8) Liddle, S. T. The Renaissance of Non-Aqueous Uranium Chemistry. *Angew. Chem., Int. Ed.* **2015**, *54*, 8604–8641.
- (9) Schädle, D.; Anwander, R. Rare-Earth Metal and Actinide Organoimide Chemistry. *Chem. Soc. Rev.* **2019**, *48*, 5752–5805.
- (10) Pauling, L. The Nature of the Chemical Bond. Application of Results Obtained from the Quantum Mechanics and from a Theory of Paramagnetic Susceptibility to the Structure of Molecules. *J. Am. Chem. Soc.* **1931**, *53*, 1367–1400.
- (11) Kerridge, A. Quantification of f-Element Covalency through Analysis of the Electron Density: Insights from Simulation. *Chem. Commun.* **2017**, *53*, 6685–6695.
- (12) Kozimor, S. A.; Yang, P.; Batista, E. R.; Boland, K. S.; Burns, C. J.; Clark, D. L.; Conradson, S. D.; Martin, R. L.; Wilkerson, M. P.; Wolfsberg, L. E. Trends in covalency for d- and f-element metallocene dichlorides identified using chlorine K-edge X-ray absorption spectroscopy and time-dependent density functional theory. *J. Am. Chem. Soc.* 2009, 131, 12125–12136.
- (13) Minasian, S. G.; Keith, J. M.; Batista, E. R.; Boland, K. S.; Clark, D. L.; Conradson, S. D.; Kozimor, S. A.; Martin, R. L.; Schwarz, D. E.; Shuh, D. K.; Wagner, G. L.; Wilkerson, M. P.; Wolfsberg, L. E.; Yang, P. Determining relative f and d orbital contributions to M-Cl covalency in MCl_6^{2-} (M = Ti, Zr, Hf, U) and $UOCl_5^{-}$ using Cl Kedge X-ray absorption spectroscopy and time-dependent density functional theory. *J. Am. Chem. Soc.* **2012**, *134*, 5586–5597.
- (14) Spencer, L. P.; Yang, P.; Minasian, S. G.; Jilek, R. E.; Batista, E. R.; Boland, K. S.; Boncella, J. M.; Conradson, S. D.; Clark, D. L.; Hayton, T. W.; Kozimor, S. A.; Martin, R. L.; MacInnes, M. M.; Olson, A. C.; Scott, B. L.; Shuh, D. K.; Wilkerson, M. P. Tetrahalide complexes of the $[U(NR)_2]^{2+}$ ion: synthesis, theory, and chlorine Kedge X-ray absorption spectroscopy. *J. Am. Chem. Soc.* **2013**, *135*, 2279–2290.
- (15) Minasian, S. G.; Keith, J. M.; Batista, E. R.; Boland, K. S.; Clark, D. L.; Kozimor, S. A.; Martin, R. L.; Shuh, D. K.; Tyliszczak, T. New evidence for 5f covalency in actinocenes determined from carbon Kedge XAS and electronic structure theory. *Chem. Sci.* **2014**, *5*, 351–359.
- (16) Cross, J. N.; Su, J.; Batista, E. R.; Cary, S. K.; Evans, W. J.; Kozimor, S. A.; Mocko, V.; Scott, B. L.; Stein, B. W.; Windorff, C. J.; Yang, P. Covalency in Americium(III) Hexachloride. *J. Am. Chem. Soc.* 2017, 139, 8667–8677.

- (17) Su, J.; Batista, E. R.; Boland, K. S.; Bone, S. E.; Bradley, J. A.; Cary, S. K.; Clark, D. L.; Conradson, S. D.; Ditter, A. S.; Kaltsoyannis, N.; Keith, J. M.; Kerridge, A.; Kozimor, S. A.; Löble, M. W.; Martin, R. L.; Minasian, S. G.; Mocko, V.; La Pierre, H. S.; Seidler, G. T.; Shuh, D. K.; Wilkerson, M. P.; Wolfsberg, L. E.; Yang, P. Energy-Degeneracy-Driven Covalency in Actinide Bonding. J. Am. Chem. Soc. 2018, 140, 17977-17984.
- (18) Smiles, D. E.; Batista, E. R.; Booth, C. H.; Clark, D. L.; Keith, J. M.; Kozimor, S. A.; Martin, R. L.; Minasian, S. G.; Shuh, D. K.; Stieber, S. C. E.; Tyliszczak, T. The duality of electron localization and covalency in lanthanide and actinide metallocenes. Chem. Sci. 2020, 11, 2796-2809.
- (19) Ganguly, G.; Sergentu, D.-C.; Autschbach, J. Ab Initio Analysis of Metal-Ligand Bonding in An(COT)2 with An = Th, U in Their Ground- and Core-Excited States. Chem.—Eur. J. 2020, 26, 1776-
- (20) Sergentu, D.-C.; Autschbach, J. Covalency in actinide(IV) hexachlorides in relation to the chlorine K-edge X-ray absorption structure. Chem. Sci. 2022, 13, 3194-3207.
- (21) Formanuik, A.; Ariciu, A.-M.; Ortu, F.; Beekmeyer, R.; Kerridge, A.; Tuna, F.; McInnes, E. J. L.; Mills, D. P. Actinide Covalency Measured by Pulsed Electron Paramagnetic Resonance Spectroscopy. Nat. Chem. 2017, 9, 578-583.
- (22) V1cha, J.; Novotny, J.; Komorovsky, S.; Straka, M.; Kaupp, M.; Marek, R. Relativistic Heavy-Neighbor-Atom Effects on NMR Shifts: Concepts and Trends across the Periodic Table. Chem. Rev. 2020, 120, 7065-7103.
- (23) For an extensive review of leading work describing the study of metal-ligand (carbon) bond covalency using NMR, see: Gordon, C. P.; Raynaud, C.; Andersen, R. A.; Copéret, C.; Eisenstein, O. Carbon-13 NMR Chemical Shift: A Descriptor for Electronic Structure and Reactivity of Organometallic Compounds. Acc. Chem. Res. 2019, 52, 2278-2289.
- (24) Hrobárik, P.; Hrobáriková, V.; Greif, A. H.; Kaupp, M. Giant Spin-Orbit Effects on NMR Shifts in Diamagnetic Actinide Complexes: Guiding the Search of Uranium(VI) Hydride Complexes in the Correct Spectral Range. Angew. Chem., Int. Ed. 2012, 51, 10884-10888.
- (25) Greif, A. H.; Hrobárik, P.; Autschbach, J.; Kaupp, M. Giant spin-orbit effects on ¹H and ¹³C NMR shifts for uranium(VI) complexes revisited: role of the exchange-correlation response kernel, bonding analyses, and new predictions. Phys. Chem. Chem. Phys. 2016, 18, 30462-30474.
- (26) Seaman, L. A.; Hrobárik, P.; Schettini, M. F.; Fortier, S.; Kaupp, M.; Hayton, T. W. A Rare Uranyl(VI)-Alkyl Ate Complex [Li(DME)_{1.5}]₂[UO₂(CH₂SiMe₃)₄] and Its Comparison with a Homoleptic Uranium(VI)-Hexaalkyl. Angew. Chem., Int. Ed. 2013, 52, 3259-3263.
- (27) Smiles, D. E.; Wu, G.; Hrobárik, P.; Hayton, T. W. Synthesis, Thermochemistry, Bonding, and ¹³C NMR Chemical Shift Analysis of a Phosphorano-Stabilized Carbene of Thorium. Organometallics 2017, 36, 4519-4524.
- (28) Rungthanaphatsophon, P.; Huang, P.; Walensky, J. R. Phosphorano-Stabilized Carbene Complexes with Short Thorium-(IV)- and Uranium(IV)-Carbon Bonds. Organometallics 2018, 37, 1884-1891.
- (29) Mullane, K. C.; Hrobárik, P.; Cheisson, T.; Manor, B. C.; Carroll, P. J.; Schelter, E. J. 13C NMR Shifts as an Indicator of U-C Bond Covalency in Uranium(VI) Acetylide Complexes: An Experimental and Computational Study. Inorg. Chem. 2019, 58, 4152-4163.
- (30) Panetti, G. B.; Sergentu, D.-C.; Gau, M. R.; Carroll, P. J.; Autschbach, J.; Walsh, P. J.; Schelter, E. J. Isolation and characterization of a covalent Ce^{IV} -Aryl complex with an anomalous ^{13}C chemical shift. Nat. Commun. 2021, 12, 1713.
- (31) Kent, G. T.; Yu, X.; Wu, G.; Autschbach, J.; Hayton, T. W. Synthesis and electronic structure analysis of the actinide allenylidene, $[\{(NR_2)_3\}An(CCCPh_2)]^-$ (An = U, Th; R = SiMe₃). Chem. Sci. **2021**, *12*, 14383–14388.

- (32) Ordoñez, O.; Yu, X.; Wu, G.; Autschbach, J.; Hayton, T. W. Homoleptic Perchlorophenyl "Ate" Complexes of Thorium(IV) and Uranium(IV). Inorg. Chem. 2021, 60, 12436-12444.
- (33) Kent, G. T.; Yu, X.; Pauly, C.; Wu, G.; Autschbach, J.; Hayton, T. W. Synthesis of Parent Acetylide and Dicarbide Complexes of Thorium and Uranium and an Examination of Their Electronic Structure. Inorg. Chem. 2021, 60, 15413-15420.
- (34) Kent, G. T.; Yu, X.; Wu, G.; Autschbach, J.; Hayton, T. W. Ring-opening of a thorium cyclopropenyl complex generates a transient thorium-bound carbene. Chem. Commun. 2022, 58, 6805-
- (35) Staun, S. L.; Sergentu, D. C.; Wu, G.; Autschbach, J.; Hayton, T. W. Use of ¹⁵N NMR Spectroscopy to Probe Covalency in a Thorium Nitride. Chem. Sci. 2019, 10, 6431-6436.
- (36) Sergentu, D. C.; Kent, G. T.; Staun, S. L.; Yu, X.; Cho, H.; Autschbach, J.; Hayton, T. W. Probing the Electronic Structure of a Thorium Nitride Complex by Solid-State ¹⁵N NMR Spectroscopy. Inorg. Chem. 2020, 59, 10138-10145.
- (37) Du, J.; Seed, J. A.; Berryman, V. E. J.; Kaltsoyannis, N.; Adams, R. W.; Lee, D.; Liddle, S. T. Exceptional Uranium(VI)-Nitride Triple Bond Covalency from ¹⁵N Nuclear Magnetic Resonance Spectroscopy and Quantum Chemical Analysis. Nat. Commun. 2021, 12, 5649.
- (38) Cho, H.; De Jong, W. A.; Soderquist, C. Z. Probing the Oxygen Environment in UO₂²⁺ by Solid-State ¹⁷O Nuclear Magnetic Resonance Spectroscopy and Relativistic Density Functional Calculations. J. Chem. Phys. 2010, 132, No. 084501.
- (39) Martel, L.; Magnani, N.; Vigier, J. F.; Boshoven, J.; Selfslag, C.; Farnan, I.; Griveau, J. C.; Somers, J.; Fanghänel, T. High-Resolution Solid-State Oxygen-17 NMR of Actinide-Bearing Compounds: An Insight into the 5f Chemistry. Inorg. Chem. 2014, 53, 6928-6933.
- (40) Martel, L.; Vigier, J.-F.; Prieur, D.; Nourry, S.; Guiot, A.; Dardenne, K.; Boshoven, J.; Somers, J. Structural Investigation of Uranium-Neptunium Mixed Oxides Using XRD, XANES, and ¹⁷O MAS NMR. J. Phys. Chem. C 2014, 118, 27640-27647.
- (41) Martel, L.; Hen, A.; Tokunaga, Y.; Kinnart, F.; Magnani, N.; Colineau, E.; Griveau, J.-C.; Caciuffo, R. Magnetization, specific heat, ¹⁷O NMR, and ²³⁷Np Mössbauer study of U_{0.15}Np_{0.85}O₂. Phys. Rev. B: Condens. Matter Mater. Phys. 2018, 98, No. 014410.
- (42) Devore, M. A.; Klug, C. A.; Kriz, M. R.; Roy, L. E.; Wellons, M. S. Investigations of Uranyl Fluoride Sesquihydrate (UO₂F₂·1.57H₂O): Combining ¹⁹F Solid-State MAS NMR Spectroscopy and GIPAW Chemical Shift Calculations. J. Phys. Chem. A 2018, 122, 6873-6878. (43) Gabuda, S. P.; Falaleeva, L. G.; Gagarinskii, Y. V. Dipolar
- Broadening of the NMR Spectrum of ¹⁹F in UF₄. Phys. Status Solidi B 1969, 33, 435-438.
- (44) Capan, C.; Dempsey, R. J.; Sinkov, S.; McNamara, B. K.; Cho, H. Probing the Pu⁴⁺ magnetic moment in PuF₄ with ¹⁹F NMR spectroscopy. Phys. Rev. B: Condens. Matter Mater. Phys. 2016, 93, No. 224409.
- (45) Martel, L.; Capelli, E.; Body, M.; Klipfel, M.; Beneš, O.; Maksoud, L.; Raison, P. E.; Suard, E.; Visscher, L.; Bessada, C.; Legein, C.; Charpentier, T.; Kovács, A. Insight into the Crystalline Structure of ThF₄ with the Combined Use of Neutron Diffraction, ¹⁹F Magic-Angle Spinning-NMR, and Density Functional Theory Calculations. Inorg. Chem. 2018, 57, 15350-15360.
- (46) Réant, B. L. L.; Berryman, V. E. J.; Basford, A. R.; Nodaraki, L. E.; Wooles, A. J.; Tuna, F.; Kaltsoyannis, N.; Mills, D. P.; Liddle, S. T. ²⁹Si NMR Spectroscopy as a Probe of s- and f-Block Metal(II)-Silanide Bond Covalency. J. Am. Chem. Soc. 2021, 143, 9813-9824.
- (47) Mounce, A. M.; Yasuoka, H.; Koutroulakis, G.; Lee, J. A.; Cho, H.; Gendron, F.; Zurek, E.; Scott, B. L.; Trujillo, J. A.; Slemmons, A. K.; Cross, J. N.; Thompson, J. D.; Kozimor, S. A.; Bauer, E. D.; Autschbach, J.; Clark, D. L. Nuclear Magnetic Resonance Measurements and Electronic Structure of Pu(IV) in [Me₄N]₂PuCl₆. Inorg. Chem. 2016, 55, 8371-8380.
- (48) Smiles, D. E.; Wu, G.; Hrobárik, P.; Hayton, T. W. Use of ⁷⁷Se and 125Te NMR Spectroscopy to Probe Covalency of the Actinide-Chalcogen Bonding in $[Th(E_n)\{N(SiMe_3)_2\}_3]^-$ (E = Se, Te; N = 1,

- 2) and Their Oxo-Uranium(VI) Congeners. J. Am. Chem. Soc. 2016, 138, 814-825.
- (49) Gardner, B. M.; Balázs, G.; Scheer, M.; Tuna, F.; McInnes, E. J. L.; McMaster, J.; Lewis, W.; Blake, A. J.; Liddle, S. T. Triamidoamine-Uranium(IV)-Stabilized Terminal Parent Phosphide and Phosphinidene Complexes. *Angew. Chem., Int. Ed.* **2014**, *53*, 4484–4488.
- (50) Behrle, A. C.; Castro, L.; Maron, L.; Walensky, J. R. Formation of a Bridging Phosphinidene Thorium Complex. *J. Am. Chem. Soc.* **2015**, 137, 14846–14849.
- (51) Behrle, A. C.; Walensky, J. R. Insertion of ^tBuNC into thorium-phosphorus and thorium-arsenic bonds: phosphaazaallene and arsaazaallene moieties in f element chemistry. *Dalton Trans.* **2016**, 45, 10042–10049.
- (52) (a) Wildman, E. P.; Balázs, G.; Wooles, A. J.; Scheer, M.; Liddle, S. T. Thorium-Phosphorus Triamidoamine Complexes Containing Th-P Single- and Multiple-Bond Interactions. *Nat. Commun.* **2016**, *7*, 12884. (b) Wildman, E. P.; Balázs, G.; Wooles, A. J.; Scheer, M.; Liddle, S. T. Author Correction: Thorium-Phosphorus Triamidoamine Complexes Containing Th-P Single- and Multiple-Bond Interactions. *Nat. Commun.* **2023**, *14*, 3045.
- (53) Rookes, T. M.; Gardner, B. M.; Balázs, G.; Gregson, M.; Tuna, F.; Wooles, A. J.; Scheer, M.; Liddle, S. T. Crystalline Diuranium-Phosphinidiide and -µ-Phosphido Complexes with Symmetric and Asymmetric UPU Cores. *Angew. Chem., Int. Ed.* **2017**, *56*, 10495–10500.
- (54) Vilanova, S. P.; Alayoglu, P.; Heidarian, M.; Huang, P.; Walensky, J. R. Metal–Ligand Multiple Bonding in Thorium Phosphorus and Thorium Arsenic Complexes. *Chem.—Eur. J.* **2017**, 23, 16748–16752.
- (55) Rungthanaphatsophon, P.; Duignan, T. J.; Myers, A. J.; Vilanova, S. P.; Barnes, C. L.; Autschbach, J.; Batista, E. R.; Yang, P.; Walensky, J. R. Influence of Substituents on the Electronic Structure of Mono- and Bis(phosphido) Thorium(IV) Complexes. *Inorg. Chem.* **2018**, *57*, 7270–7278.
- (56) Zhang, C.; Hou, G.; Zi, G.; Ding, W.; Walter, M. D. A Base-Free Terminal Actinide Phosphinidene Metallocene: Synthesis, Structure, Reactivity, and Computational Studies. *J. Am. Chem. Soc.* **2018**, *140*, 14511–14525.
- (57) Rookes, T. M.; Wildman, E. P.; Balázs, G.; Gardner, B. M.; Wooles, A. J.; Gregson, M.; Tuna, F.; Scheer, M.; Liddle, S. T. Actinide-Pnictide (An-Pn) Bonds Spanning Non-Metal, Metalloid, and Metal Combinations (An = U, Th; Pn = P, As, Sb, Bi). *Angew. Chem., Int. Ed.* **2018**, *57*, 1332–1336.
- (58) Zhang, C.; Hou, G.; Zi, G.; Walter, M. D. A base-free terminal thorium phosphinidene metallocene and its reactivity toward selected organic molecules. *Dalton Trans.* **2019**, *48*, 2377–2387.
- (59) Zhang, C.; Hou, G.; Zi, G.; Ding, W.; Walter, M. D. An Alkali-Metal Halide-Bridged Actinide Phosphinidiide Complex. *Inorg. Chem.* **2019**, *58*, 1571–1590.
- (60) Wang, Y.; Zhang, C.; Zi, G.; Ding, W.; Walter, M. D. Preparation of a potassium chloride bridged thorium phosphinidiide complex and its reactivity towards small organic molecules. *New J. Chem.* **2019**, 43, 9527.
- (61) Wang, D.; Ding, W.; Hou, G.; Zi, G.; Walter, M. D. Experimental and Computational Studies on a Base-Free Terminal Uranium Phosphinidene Metallocene. *Chem.—Eur. J.* **2020**, 26, 16888–16899.
- (62) Wang, D.; Wang, S.; Hou, G.; Zi, G.; Walter, M. D. A Lewis Base Supported Terminal Uranium Phosphinidene Metallocene. *Inorg. Chem.* **2020**, *59*, 14549–14563.
- (63) Wang, D.; Hou, G.; Zi, G.; Walter, M. D. $(\eta^5 C_3 Me_5)_2 U (=P-2,4,6-{}^tBu_3C_6H_2)(OPMe_3)$ Revisited Its Intrinsic Reactivity toward Small Organic Molecules. *Organometallics* **2020**, *39*, 4085–4101.
- (64) Du, J.; Hunger, D.; Seed, J. A.; Cryer, J. D.; King, D. M.; Wooles, A. J.; Van Slageren, J.; Liddle, S. T. Dipnictogen f-Element Chemistry: A Diphosphorus Uranium Complex. J. Am. Chem. Soc. 2021, 143, 5343–5348.
- (65) Wang, D.; Hou, G.; Zi, G.; Walter, M. D. Influence of the Lewis Base Ph₃PO on the Reactivity of the Uranium Phosphinidene (η^5 -

- C_5Me_5 ₂U(=P-2,4,6- i Pr₃C₆H₂)(OPPh₃). Organometallics **2021**, 40, 383–396.
- (66) Wang, S.; Li, T.; Heng, Y.; Hou, G.; Zi, G.; Walter, M. D. Influence of the 1,3-Bis(trimethylsilyl)cyclopentadienyl Ligand on the Reactivity of the Uranium Phosphinidene $[\eta^5$ -1,3- $(Me_3Si)_2C_5H_3]_2U$ - $(=P-2,4,6-iPr_3C_6H_2)(OPPh_3)$. Organometallics 2021, 40, 2149–2165.
- (67) Tarlton, M. L.; Yang, Y.; Kelley, S. P.; Maron, L.; Walensky, J. R. Formation and Reactivity with 'BuCN of a Thorium Phosphinidiide through a Combined Experimental and Computational Analysis. *Organometallics* **2021**, *40*, 2701–2708.
- (68) Wang, D.; Wang, S.; Li, T.; Heng, Y.; Hou, G.; Zi, G.; Walter, M. D. Reactivity studies involving a Lewis base supported terminal uranium phosphinidene metallocene $[\eta^5-1,3-(Me_3C)_2C_5H_3]_2U(=P-2,4,6^-iPr_3C_6H_2)(OPMe_3)$. Dalton Trans. **2021**, 50, 8349–8363.
- (69) Tarlton, M. L.; Fajen, O. J.; Kelley, S. P.; Kerridge, A.; Malcomson, T.; Morrison, T. L.; Shores, M. P.; Xhani, X.; Walensky, J. R. Systematic Investigation of the Molecular and Electronic Structure of Thorium and Uranium Phosphorus and Arsenic Complexes. *Inorg. Chem.* **2021**, *60*, 10614–10630.
- (70) Tarlton, M. L.; Vilanova, S. P.; Kaumini, M. G.; Kelley, S. P.; Huang, P.; Walensky, J. R. Structural, Spectroscopic, and Computational Analysis of Heterometallic Thorium Phosphinidiide Complexes. *Inorg. Chem.* **2021**, *60*, 14932–14943.
- (71) Du, J.; Balazs, G.; Seed, J. A.; Cryer, J. D.; Wooles, A. J.; Scheer, M.; Liddle, S. T. Actinide Pnictinidene Chemistry: A Terminal Thorium Parent-Arsinidene Complex Stabilised by a Super-Bulky Triamidoamine Ligand. *Angew. Chem., Int. Ed.* **2022**, *61*, No. e202211627.
- (72) Eichele, K.; Wasylishen, R. E.; Corrigan, J. F.; Taylor, N. J.; Carty, A. J. Phosphorus-31 Chemical Schift Tensors of Phosphinidene Ligands in Ruthenium Carbonyl Cluster Compounds: A ³¹P Single-Crystal and CP/MAS-NMR Study. *J. Am. Chem. Soc.* **1995**, *117*, 6961–6969.
- (73) Zhao, G.; Basuli, F.; Kilgore, U. J.; Fan, H.; Aneetha, H.; Huffman, J. C.; Wu, G.; Mindiola, D. J. Neutral and Zwitterionic Low-Coordinate Titanium Complexes Bearing the Terminal Phosphinidene Functionality. Structural, Spectroscopic, Theoretical, and Catalytic Studies Addressing the Ti-P Multiple Bond. *J. Am. Chem. Soc.* 2006, 128, 13575–13585.
- (74) Wu, G.; Rovnyak, D.; Johnson, M. J. A.; Zanetti, N. C.; Musaev, D. G.; Morokuma, K.; Schrock, R. R.; Griffin, R. G.; Cummins, C. C. Unusual ³¹P Chemical Shielding Tensors in Terminal Phosphido Complexes Containing a Phosphorus-Metal Triple Bond. *J. Am. Chem. Soc.* **1996**, *118*, 10654–10655.
- (75) Zanetti, N. C.; Schrock, R. R.; Davis, W. M. Monomeric Molbdenum and Tungsten Complexes That Contain a Metal-Phosphorus Triple Bond. *Angew. Chem., Int. Ed.* **1995**, 34, 2044—2046.
- (76) Laplaza, C. E.; Davis, W. M.; Cummins, C. C. A Molybdenum-Phosphorus Triple Bond: Synthesis, Structure, and Reactivity of the Terminal Phosphido (P³⁻) Complex [Mo(P)(NRAr)₃]. *Angew. Chem., Int. Ed.* **1995**, 34, 2042–2044.
- (77) Halbert, S.; Copéret, C.; Raynaud, C.; Eisenstein, O. Elucidating the Link Betweeen NMR Chemical Shifts and Electronic Structure in d⁰ Olefin Metathesis Catalysts. *J. Am. Chem. Soc.* **2016**, 138, 2261–2272.
- (78) Ramsey, N. F. Magnetic Shielding of Nuclei in Molecules. *Phys. Rev.* 1950, 78, 699-703.
- (79) Ramsey, N. F. Dependence of Magnetic Shielding of Nuclei upon Molecular Orientation. *Phys. Rev.* **1951**, *83*, 540–541.
- (80) Ramsey, N. F. Chemical Effects in Nuclear Magnetic Resonance and in Diamagnetic Susceptibility. *Phys. Rev.* **1952**, *86*, 243–246.
- (81) Widdifield, C. M.; Schurko, R. W. Understanding Chemical Shielding Tensors Using Group Theory, MO Analysis, and Modern Density-Functional Theory. *Concepts in Magnetic Resonance Part A* **2009**, 34A, 91–123.

- (82) Sutter, K.; Autschbach, J. Computational Study and Molecular Orbital Analysis of NMR Shielding, Spin-Spin Coupling, and Electric Field Gradients of Azido Platinum Complexes. J. Am. Chem. Soc. 2012, 134, 13374—13385.
- (83) Payard, P.-A.; Perego, L. A.; Grimaud, L.; Ciofini, I. A DFT Protocol for the Prediction of ³¹P NMR Chemical Shifts of Phosphine Ligands in First-Row Transition-Metal Complexes. *Organometallics* **2020**, *39*, 3121–3130.
- (84) Raynaud, C.; Norbert-Agaisse, E.; James, B. R.; Eisenstein, O. ³¹P Chemical Shifts in Ru(II) Phosphine Complexes. A Computational Study of the Influence of the Coordination Sphere. *Inorg. Chem.* **2020**, *59*, 17038–17048.
- (85) Transue, W. J.; Dai, Y.; Riu, M. -L. Y.; Wu, G.; Cummins, C. C. ³¹P NMR Chemical Shift Tensors: Windows into Ruthenium Phosphinidene Complex Electronic Structures. *Inorg. Chem.* **2021**, 60, 9254–9258.
- (86) Kondrashova, S. A.; Polyancev, F. M.; Latypov, S. K. DFT Calculations of ³¹P NMR Chemical Shifts in Palladium Complexes. *Molecules* **2022**, 27, 2668.
- (87) Autschbach, J. Analyzing NMR Shielding Tensors Calculated with Two-Component Relativistic Methods Using Spin-Free Localized Molecular Orbitals. *J. Chem. Phys.* **2008**, *128*, No. 164112.
- (88) Autschbach, J.; Zheng, S. Analyzing Pt Chemical Shifts Calculated from Relativistic Density Functional Theory using Localized Orbitals: The Role of Pt 5d Lone Pairs. *Magn. Reson. Chem.* **2008**, *46*, S45–S55.
- (89) Wicker, B. F.; Scott, J.; Andino, J. G.; Gao, X.; Park, H.; Pink, M.; Mindiola, D. J. Phosphinidene Complexes of Scandium: Powerful Par Group-Transfer Vehicles to Organic and Inorganic Substrates. *J. Am. Chem. Soc.* **2010**, *132*, 3691–3693.
- (90) Feng, B.; Xiang, L.; Carpentier, A.; Maron, L.; Leng, X.; Chen, Y. Scandium-Terminal Boronylphosphinidene Complex. *J. Am. Chem. Soc.* **2021**, *143*, 2705–2709.
- (91) Basuli, F.; Tomaszewski, J.; Huffman, J. C.; Mindiola, D. J. Four-Coordinate Phosphinidene Complexes of Titanium Prepared by α -H-Migration: Phospha-Staudinger and Phosphaalkene-Insertion Reactions. *J. Am. Chem. Soc.* **2003**, *125*, 10170–10171.
- (92) Bailey, B. C.; Huffman, J. C.; Mindiola, D. J.; Weng, W.; Ozerov, O. V. Remarkably Stable Titanium Complexes Containing Terminal Alkylidene, Phosphinidene, and Imide Functionalities. *Organometallics* **2005**, *24*, 1390–1393.
- (93) Fischer, M.; Reiß, F.; Hering-Junghans, C. Titanocene pnictinidene complexes. *Chem. Commun.* **2021**, *57*, 5626–5629.
- (94) Pikies, J.; Baum, E.; Matern, E.; Chojnacki, J.ła.; Grubba, R.ł; Robaszkiewicz, A. A new synthetic entry to phosphinophosphinidene complexes. Synthesis and structural characterisation of the first side-on bonded and the first terminally bonded phosphinophosphinidene zirconium complexes $[\mu-(1,2:2-\eta-{}^{t}Bu_{2}P=P)\{Zr(Cl)Cp_{2}\}_{2}]$ and $[\{Zr(PPhMe_{2})Cp_{2}\}(\eta^{1}-P-P^{t}Bu_{2})]$. Chem. Commun. **2004**, 2478–2479.
- (95) Stafford, H.; Rookes, T. M.; Wildman, E. P.; Balázs, G.; Wooles, A. J.; Scheer, M.; Liddle, S. T. Terminal Parent Phosphanide and Phosphinidene Complexes of Zirconium(IV). *Angew. Chem., Int. Ed.* **2017**, *56*, 7669–7673.
- (96) Buss, J. A.; Hirahara, M.; Ueda, Y.; Agapie, T. Molecular Mimics of Heterogeneous Metal Phosphides: Thermochemistry, Hydride-Proton Isomerism, and HER Reactivity. *Angew. Chem., Int. Ed.* **2018**, *57*, 16329–16333.
- (97) Kramkowski, P.; Scheer, M. Naked" Phosphorus as a Bent Bridging Ligand. *Angew. Chem., Int. Ed.* **2000**, *39*, 928–931.
- (98) Scheer, M.; Müller, J.; Baum, G.; Häser, M. Reaction behaviour of a complex containing a tungsten phosphorus triple bond with σ -acceptor compounds of group 13. *Chem. Commun.* **1998**, 1051–1052.
- (99) Balázs, G.; Hautmann, M.; Seidl, M.; Scheer, M. Reactivity of $[(N_3)W\equiv P]$ towards gold(I) salts synthesis of $[(N_3N)W\equiv P-AuCl]$ and $[\{(N_3N)W\equiv P\}_2Au][pftb]$ (pftb = Al(OC(CF₃)₃)₄. *Inorg. Chim. Acta* 2018, 475, 47–52.

- (100) Figueroa, J. S.; Cummins, C. C. Diorganophosphanylphosphinidenes as Complexed Ligands: Synthesis via an Anionic Terminal Phosphide of Niobium. *Angew. Chem., Int. Ed.* **2004**, *43*, 984–988.
- (101) Cherry, J. -P. F.; Johnson, A. R.; Baraldo, L. M.; Tsai, Y.-C.; Cummins, C. C.; Kryatov, S. V.; Rybak-Akimova, E. V.; Capps, K. B.; Hoff, C. D.; Haar, C. M.; Nolan, S. P. On the Origin of Selective Nitrous Oxide N-N Bond Cleavage by Three-Coordinate Molybdenum(III) Complexes. *J. Am. Chem. Soc.* **2001**, *123*, 7271–7286.
- (102) Cherry, J. -P. F.; Stephens, F. H.; Johnson, M. J. A.; Diaconescu, P. L.; Cummins, C. C. Terminal Phosphide and Dinitrogen Molybdenum Compounds Obtained from Pnictide-Bridged Precursors. *J. Am. Chem. Soc.* **2001**, *40*, 6860–6862.
- (103) Stephens, F. H.; Figueroa, J. S.; Diaconescu, P. L.; Cummins, C. C. Molybdenum-Phosphorus Triple Bond Stabilization by Ancullary Alkoxide Ligation: Synthesis and Structure of a Terminal Phosphide Tris-1-methylcyclohexanoxide Complex. *J. Am. Chem. Soc.* **2003**, *125*, 9264–9265.
- (104) Buss, J. A.; Oyala, P. H.; Agapie, T. Terminal Molybdenum Phosphides with d Electrons: Radical Character Promotes Coupling Chemistry. *Angew. Chem., Int. Ed.* **2017**, *56*, 14502–14506.
- (105) Fox, A. R.; Clough, C. R.; Piro, N. A.; Cummins, C. C. A Terminal Nitride-to-Phosphide Conversion Sequence Followed by Tungsten Phosphide Functionalization Using a Diphenylphosphenium Synthon. *Angew. Chem., Int. Ed.* **2007**, *46*, 973–976.
- (106) Joost, M.; Transue, W. J.; Cummins, C. C. Terminal tungsten pnictide complex formation through pnictaethynolate decarbonylation. *Chem. Commun.* **2017**, *53*, 10731–10733.
- (107) Abbenseth, J.; Diefenbach, M.; Hinz, A.; Alig, L.; Würtele, C.; Goicoechea, J. M.; Holthausen, M. C.; Schneider, S. Oxidative Coupling of Terminal Rhenium Pnictide Complexes. *Angew. Chem., Int. Ed.* **2019**, *58*, 10966–10907.
- (108) Hitchcock, P. B.; Lappert, M. F.; Leung, W.-P. The First Stable Transition Metal (Molybdenum or Tungsten) Complexes Having a Metal-Phosphorus(III) Double Bond: the Phosphorus Analogues of Metal Aryl- and Alkyl-imides; X-Ray Structure of $\left[Mo(\eta\text{-}C_5H_5)_2(=PAr)\right]$ (Ar = $C_6H_2Bu^t_3$ -2,4,6). J. Chem. Soc. Chem. Commun. 1987, 1282–1283.
- (109) Edwards, P. G.; Andersen, R. A.; Zalkin, A. Preeparation of Tetraalkyl Phosphine Complexes of the f-Block Metals. Crystal Structure of Th(CH₂Ph)₄(Me₂PCH₂CH₂PMe₂) and U(CH₂Ph)₃Me-(Me₂PCH₂CH₂PMe₂). Organometallics **1984**, *3*, 293–298.
- (110) Termaten, A. T.; Schakel, M.; Ehlers, A. W.; Lutz, M.; Spek, A. L.; Lammertsma, K. N-Heterocyclic Carbene Functionalized Iridium Phosphinidene Complex [Cp*(NHC)Ir = PMes*]: Comparison of Phosphinidene, Imido, and Carbene Complexes. *Chem.—Eur. J.* **2003**, 9. 3577—3582.
- (111) Menye-Biyogo, R.; Delpech, F.; Castel, A.; Gornitzka, H.; Rivière, P. Ruthenium-Stabilized Low-Coordinate Phosphorus Atoms: Structural Evidence for Monomeric Metaphosphonate. *Angew. Chem., Int. Ed.* **2003**, *42*, 5610–5612.
- (112) Termaten, A. T.; Nijbacker, T.; Schakel, M.; Lutz, M.; Spek, A. L.; Lammertsma, K. Synthesis and Reactions of Terminal Osmium and Ruthenium Complexed Phosphinidenes $[(\eta^6\text{-Ar})(L)M = PMes^*]$. Chem.—Eur. J. 2003, 9, 2200–2208.
- (113) Abbenseth, J.; Schneider, S. A Terminal Chlorophosphinidene Complex. Z. Anorg. Allg. Chem. 2020, 646, 565–569.
- (114) Melenkivitz, R.; Mindiola, D. J.; Hillhouse, G. L. Monomeric Phosphido and Phosphinidene Complexes of Nickel. *J. Am. Chem. Soc.* **2002**, *124*, 3846–3847.
- (115) Aktas, H.; Slootweg, J. C.; Ehlers, A. W.; Lutz, M.; Spek, A. L.; Lammertsma, K. N-Heterocyclic Carbene Functionalized Group 7–9 Transition Metal Phosphinidene Complexes. *Organometallics* **2009**, 28, 5166–5172.
- (116) Termaten, A. T.; Nijbacker, T.; Schakel, M.; Lutz, M.; Spek, A. L.; Lammertsma, K. Synthesis of Novel Terminal Iridium Phosphinidene Complexes. *Organometallics* **2002**, *21*, 3196–3202.
- (117) Termaten, A. T.; Aktas, H.; Schakel, M.; Ehlers, A. W.; Lutz, M.; Spek, A. L.; Lammertsma, K. Terminal Phosphinidene Complexes

- Cp^R(L)M = PAr of the Group 9 Transition Metals Cobalt, Rhodium, and Iridium. Synthesis, Structures, and Properties. *Organometallics* **2003**, 22, 1827–1834.
- (118) Fonseca Guerra, C.; Snijders, J. G.; Te Velde, G.; Baerends, E. J. Towards an Order-N DFT Method. *Theor. Chem. Acc.* **1998**, 99, 391–403.
- (119) Te Velde, G.; Bickelhaupt, F. M.; Baerends, E. J.; Fonseca Guerra, C.; van Gisbergen, S. J. A.; Snijders, J. G.; Ziegler, T. Chemistry with ADF. *J. Comput. Chem.* **2001**, *22*, 931–967.
- (120) van Lenthe, E.; Baerends, E. J.; Snijders, J. G. Relativistic Regular Two-Component Hamiltonians. *J. Chem. Phys.* **1993**, *99*, 4597–4610.
- (121) Van Lenthe, E.; Baerends, E. J.; Snijders, J. G. Relativistic Total Energy Using Regular Approximations. *J. Chem. Phys.* **1994**, *101*, 9783–9792.
- (122) Van Lenthe, E.; Ehlers, A. E.; Baerends, E. J. Geometry Optimization in the Zero Order Regular Approximation for Relativistic Effects. *J. Chem. Phys.* **1999**, *110*, 8943–8953.
- (123) Vosko, S. H.; Wilk, L.; Nusair, M. Accurate Spin-Dependent Electron Liquid Correlation Energies for Local Spin Density Calculations: A Critical Analysis. *Can. J. Phys.* **1980**, 58, 1200–1211.
- (124) Becke, A. D. Density-Functional Exchange-Energy Approximation with Correct Asymptotic Behaviour. *Phys. Rev. A* **1988**, *38*, 3098
- (125) Perdew, J. P. Density-Functional Approximation for the Correlation Energy of the Inhomogeneous Electron Gas. *Phys. Rev. B* **1986**, 33, 8822.
- (126) Glendening, E. D.; Landis, C. R.; Weinhold, F. NBO 6.0: Natural Bond Orbital Analysis Program. *J. Comput. Chem.* **2013**, 34, 2134–2134.
- (127) Schreckenbach, G.; Ziegler, T. Calculation of NMR Shielding Tensors Using Gauge-Including Atomic Orbitals and Modern Density Functional Theory. *J. Phys. Chem.* **1995**, *99*, 606–611.
- (128) Autschbach, J.; Zurek, E. Relativistic Density-Functional Computations of the Chemical Shift of 129 Xe in Xe@C₆₀. *J. Phys. Chem. A* **2003**, 107, 4967–4972.
- (129) Krykunov, M.; Ziegler, T.; van Lenthe, E. Hybrid Density Functional Calculations of Nuclear Magnetic Shieldings using Slater-Type Orbitals and the Zeroth-Order Regular Approximation. *Int. J. Quantum Chem.* **2009**, *109*, *1676*–1683.
- (130) Wolff, S. K.; Ziegler, T.; Van Lenthe, E.; Baerends, E. J. Density Functional Calculations of Nuclear Magnetic Shieldings Using the Zeroth-Order Regular Approximation (ZORA) for Relativistic Effects: ZORA Nuclear Magnetic Resonance. *J. Chem. Phys.* 1999, 110, 7689–7698.
- (131) Autschbach, J. The Role of the Exchange-Correlation Response Kernel and Scaling Corrections in Relativistic Density Functional Nuclear Magnetic Shielding Calculations with the Zeroth-Order Regular Approximation. *Mol. Phys.* 2013, 111, 2544–2554.
- (132) Van Wüllen, C. A comparison of density functional methods for the calculation of phosphorus-31 NMR chemical shifts. *Phys. Chem. Chem. Phys.* **2000**, *2*, 2137–2144.
- (133) Maryasin, B.; Zipse, H. Theoretical studies of ³¹P NMR spectral properties of phosphanes and related compounds in solution. *Phys. Chem. Chem. Phys.* **2011**, *13*, 5150–5158.
- (134) Latypov, S. K.; Polyancev, F. M.; Yakhvarov, D. G.; Sinyashin, O. G. Quantum chemical calculations of ³¹P NMR chemical shifts: scopes and limitations. *Phys. Chem. Chem. Phys.* **2015**, *17*, 6976–6987.
- (135) Young, R. P.; Lewis, C. R.; Yang, C.; Wang, L.; Harper, J. K.; Mueller, L. J. TensorView: A Software Tool for Displaying NMR Tensors. *Magn. Reson. Chem.* **2019**, *57*, 211–223.